

The Giant Molecular Cloud G148.24+00.41: Gas Properties, Kinematics, and Cluster Formation at the Nexus of Filamentary Flows

Vineet Rawat,^{1,2}★ M. R. Samal,¹ D. L. Walker,³ D.K. Ojha,⁴ A. Tej,⁵ A. Zavagno,^{6,7} C.P. Zhang,^{8,9} Davide Elia,¹⁰ S. Dutta,¹¹ J. Jose,¹² C. Eswaraiah,¹² E. Sharma,¹

¹Physical Research Laboratory, Navrangpura, Ahmedabad, Gujarat 380009, India

²Indian Institute of Technology Gandhinagar Palaj, Gandhinagar 382355, India

³Jodrell Bank Centre for Astrophysics, Department of Physics and Astronomy, University of Manchester, Oxford Road, Manchester M13 9PL, UK

⁴Department of Astronomy and Astrophysics, Tata Institute of Fundamental Research, Mumbai 400005, India

⁵Indian Institute of Space Science and Technology (IIST), Thiruvananthapuram 695 547, Kerala, India

⁶Aix-Marseille Universite, CNRS, CNES, LAM, 38 rue F. Joliot Curie, 13388 Marseille Cedex 13, France

⁷Institut Universitaire de France, Paris, 1 rue Descartes, 75231 Paris Cedex 05, France

⁸National Astronomical Observatories, Chinese Academy of Sciences, Beijing 100101, People's Republic of China

⁹Guizhou Radio Astronomical Observatory, Guizhou University, Guiyang 550000, People's Republic of China

¹⁰Istituto di Astrofisica e Planetologia Spaziali, INAF, Via Fosso del Cavaliere 100, I-00133 Roma, Italy

¹¹Institute of Astronomy and Astrophysics, Academia Sinica, Roosevelt Rd, Taipei 10617, Taiwan, R.O.C.

¹²Indian Institute of Science Education and Research (IISER) Tirupati, Rami Reddy Nagar, Karakambadi Road, Tirupati 517 507, India

9 January 2024

ABSTRACT

Filamentary flows toward the centre of molecular clouds have been recognized as a crucial process in the formation and evolution of stellar clusters. In this paper, we present a comprehensive observational study that investigates the gas properties and kinematics of the Giant Molecular Cloud G148.24+00.41 using the observations of CO (1-0) isotopologues. We find that the cloud is massive ($10^5 M_\odot$) and is one of the most massive clouds of the outer Galaxy. We identified six likely velocity coherent filaments in the cloud having length, width, and mass in the range of 14–38 pc, 2.5–4.2 pc, and $(1.3\text{--}6.9) \times 10^3 M_\odot$, respectively. We find that the filaments are converging towards the central area of the cloud, and the longitudinal accretion flows along the filaments are in the range of $\sim 26\text{--}264 M_\odot \text{ Myr}^{-1}$. The cloud has fragmented into 7 clumps having mass in the range of $\sim 260\text{--}2100 M_\odot$ and average size around ~ 1.4 pc, out of which the most massive clump is located at the hub of the filamentary structures, near the geometric centre of the cloud. Three filaments are found to be directly connected to the massive clump and transferring matter at a rate of $\sim 675 M_\odot \text{ Myr}^{-1}$. The clump hosts a near-infrared cluster. Our results show that large-scale filamentary accretion flows towards the central region of the collapsing cloud is an important mechanism for supplying the matter necessary to form the central high-mass clump and subsequent stellar cluster.

Key words: stars: formation; ISM: clouds; galaxies: star clusters, general; ISM: molecules; molecular data

1 INTRODUCTION

It is largely established that a large fraction of stars form in stellar clusters (Lada & Lada 2003). However, how exactly stellar clusters form, in particular intermediate to high-mass clusters, remains largely unknown and has been the subject of several recent reviews (Longmore et al. 2014; Krumholz et al. 2019; Krause et al. 2020; Adamo et al. 2020). Massive to intermediate-mass clusters play an important role in the evolution and chemical enrichment of the Galaxy through radiation and winds. As they contain a large number of stars from the same parental cloud, they also serve as an important astrophys-

ical laboratory for studying the stellar initial mass function, stellar evolution, and stellar dynamics.

The different mechanisms which have been proposed for cluster formation are *monolithic* collapse mode and flow-driven models like *global hierarchical collapse* (GHC; Vázquez-Semadeni et al. 2019) and *inertial inflow* (I2; Padoan et al. 2020). In the *monolithic* mode, a sufficient amount of gas is hypothesized to be condensed into the cluster volume before star formation commences and thus predicts the formation of a massive clump before the onset of star formation (Banerjee & Kroupa 2015). In flow-driven models, the matter flows hierarchically in the cloud from large-scale regions down to its collapse centre in a ‘conveyor belt’ fashion, eventually forming a stellar cluster at the bottom of the potential of the cloud (Longmore et al. 2014; Walker et al. 2016; Barnes et al. 2019; Vázquez-Semadeni

★ E-mail: vineet@prl.res.in

et al. 2019; Krumholz & McKee 2020). In this multi-scale dynamical mass transfer, each level in the hierarchy of density structures is accreting from its parent structure.

Understanding the dominant mode(s) of massive cluster formation requires studying massive molecular clouds that are at the early stages of their evolution, because i) a massive bound cloud with a significant dense gas reservoir is required to form a high-mass cluster, and ii) once star formation is underway, the massive members of the cluster can erase/alter the initial conditions and structure of the parental gas on a very short timescale via feedbacks such as radiation, jets, and stellar winds.

Over the last decade, various dust continuum and molecular line observations suggest that the interstellar medium is filamentary, consisting of filamentary structures of different shapes and sizes at all scales (André et al. 2010; Molinari et al. 2010; Schisano et al. 2014; Shimajiri et al. 2019; Liu et al. 2021; Li et al. 2022; Zavagno et al. 2023). Depending on densities and scales, they are often called filaments, fibres, and streamers (for details, see review articles by Hacar et al. 2022; Pineda et al. 2022). The filaments are the preferred sites of active star formation (Könyves et al. 2015; André 2017), with high-mass stars and stellar clusters preferentially forming in the high-density regions of the clouds such as hubs and ridges (Myers 2009; Motte et al. 2018; Kumar et al. 2020, 2022; Beltrán et al. 2022; Yang et al. 2023; Zhang et al. 2023), where converging flows found to be funnelling the cold matter to the hub through the filamentary networks (e.g. Schneider et al. 2010; Treviño-Morales et al. 2019). Thus, evaluating the physical conditions of the gas in molecular clouds and characterizing structures, such as filaments, ridges, and hubs, and investigating their kinematics using molecular line data, are crucial steps for understanding the evolution of molecular clouds and associated cluster formation.

In a recent work, Rawat et al. (2023) characterized and investigated one such aforementioned type of cloud, "G148.24+00.41", in order to find out its cluster formation potential and mechanism(s) by which an eventual cluster may emerge. Rawat et al. (2023) found that G148.24+00.41 is a bound, massive (mass $\sim 10^5 M_\odot$), and cold (dust temperature ~ 14.5 K) giant molecular cloud (GMC) located at a kinematic distance of $\sim 3.4 \pm 0.3$ kpc. The cloud is still in the early stages of its evolution, such that stellar feedback is not yet significant. Comparing with nearby molecular clouds as well as the massive clouds of the Galactic centre, they conclude that the total gas mass content and dense gas fraction ($\sim 18\%$) of G148.24+00.41 is similar to the Orion-A cloud (Lada et al. 2010). Based on *Herschel* observations, Rawat et al. (2023) visually identified several large-scale (5–10 pc) filament-like structures (shown in Fig. 1) in the cloud, which appear to merge near the geometric centre of the cloud. This configuration is found to resemble the hub-filamentary systems of molecular clouds (e.g. Myers 2009), where star-cluster formation takes place. Using *Spitzer* mid-infrared images, the authors observed the presence of an embedded cluster at the hub location (shown in Fig. 1). The cluster is not visible in optical and barely visible in near-infrared 2MASS images, suggesting that the young cluster is still forming. The cluster location corresponds to an Infrared source, RAFGL 5107, identified by IRAS based on far-infrared observations (Wouterloot & Brand 1989). Using various observational metrics of the cloud (such as enclosed mass over radius, density profile, fractalness, spatial and temporal distribution of protostars, degree and scales of mass-segregation, and distribution and structure of the cold gas) and comparing them with the prediction of aforementioned models of cluster formation, Rawat et al. (2023) argue that the cloud has the potential to make an intermediate to high-mass cluster through the

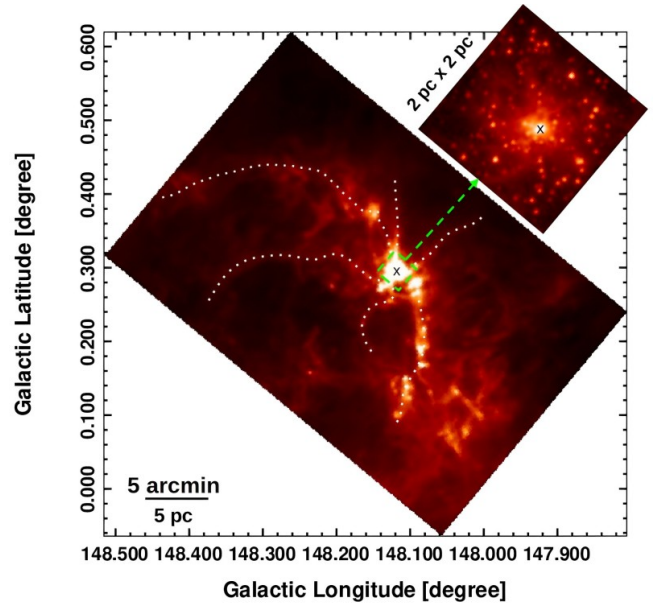


Figure 1. Central area of the G148.24+00.41 cloud as seen in *Herschel* 250 μm band, showing the hub-filamentary morphology. The inset image shows the presence of an embedded cluster within the hub region (shown by a green box) at 3.6 μm . The filamentary structures are from Rawat et al. (2023). We note that for a better presentation of the molecular data, in this work, this figure, as well as the subsequent figures, are presented in the galactic coordinates, whereas figures of Rawat et al. (2023) are in the FK5 system.

hierarchical assembly of both gas and stars, such as those predicated in conveyor-belt type models.

Rawat et al. (2023), based on dust continuum and stellar content analyses, proposed that G148.24+00.41 has the potential to make a rich cluster, preferentially at the hub location. The physical and kinematic structure of gas in GMCs is typically complex due to the interplay of turbulence and gravity. Gas kinematics provides a diagnostic tool for understanding the physical processes involved in the conversion of gas mass into stellar mass. In this work, using low spatial resolution molecular line data of CO (1–0) isotopologues, we explore 1-square degree area centred around the hub of G148.24+00.41, and present the first detailed study of large-scale gas properties and kinematics of the various structures associated with the cloud. We aim to understand the gas assembly processes from cloud-scale to clump-scale; thus, the role of the gaseous structures in the formation of the stars or star clusters as evidenced in the cloud by Rawat et al. (2023).

We organize this paper as follows. In Section 2, we describe the data used in this work. In Section 3, we present the global gas properties and kinematics of G148.24+00.41, and compare our results with the nearby Galactic clouds. In Section 3.3, we discuss the clumps of the cloud and their properties. In Section 3.2, we discuss filamentary structures, their extraction, properties, and the gas kinematics along the filaments. We also present the measured longitudinal gas mass accretion rate along the filaments. In Section 4, we discuss our results in the context of cluster formation scenario in the G148.24+00.41 cloud and summarize our findings in Section 5.

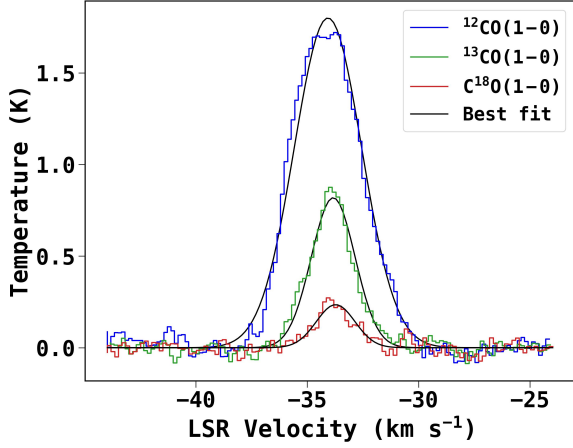


Figure 2. The average ^{12}CO , ^{13}CO , and C^{18}O spectral profiles towards the direction of the G148.24+00.41 cloud. The black solid curve shows the Gaussian fit over the spectra.

2 DATA

The molecular line observations of the G148.24+00.41 complex in ^{12}CO , ^{13}CO , and C^{18}O lines ($J = 1-0$ transitions) at 115.271, 110.201, and 109.782 GHz, respectively, were observed with the 13.7-m radio telescope as part of the Milky Way Imaging Scroll Painting (MWISP; Su et al. 2019) survey, led by the Purple Mountain Observatory (PMO). The MWISP survey mapping covers the Galactic longitude from $l = 9^\circ.75$ to $230^\circ.25$ and the Galactic latitude from $b = -5^\circ.25$ to $5^\circ.25$. The three CO isotopologue line observations were done simultaneously using a 3×3 beam sideband-separating Superconducting Spectroscopic Array Receiver (SSAR) system (Shan et al. 2012) and using the position-switch on-the-fly mode, scanning the region at a rate of $50''$ per second. The calibration was done using the standard chopping wheel method that allows switching between the sky and an ambient temperature load. The calibrated data were then re-gridded to $30''$ pixels and mosaicked to a FITS cube using the GILDAS software package (Guilloteau & Lucas 2000). The antenna temperature (T_A) has been converted to the main-beam temperature (T_{MB}) using the relation $T_{\text{MB}} = T_A/B_{\text{eff}}$, where B_{eff} is the beam efficiency, which is 46% at 115 GHz and 49% at 110 GHz. The spatial resolutions (Half Power Beam Width; HPBW) of the observations are around $\sim 49''$, $52''$, and $52''$ for ^{12}CO , ^{13}CO , and C^{18}O , respectively, which correspond to a spatial resolution of $\sim 0.8-0.9$ pc at the distance of the cloud (~ 3.4 kpc). The spectral resolution of ^{12}CO is ~ 0.16 km s $^{-1}$ with a typical rms noise level of the spectral channel is about 0.5 K, and of ^{13}CO and C^{18}O is ~ 0.17 km s $^{-1}$ with a rms noise level of 0.3 K (for details, see Su et al. 2019).

3 RESULTS AND ANALYSIS

The advantage of using the CO ($1-0$) isotopologues is that one can use the ^{12}CO emission to trace the enveloping layer (i.e. $\sim 10^2$ cm $^{-3}$) of the molecular cloud to reveal its large-scale low surface brightness structures and dynamics. On the other hand, the optically thin ^{13}CO and C^{18}O emission (discussed in Section 3.1.2) can trace the denser regions (i.e. $\sim 10^3-10^4$ cm $^{-3}$) such as large-scale filamentary structure and dense clumps within the cloud. By combining the CO isotopologues, the overall properties of the diffuse regions of the

cloud, as well as the gas properties and physical conditions of the dense structures within it, can be determined.

3.1 Global Cloud Morphology, Properties, and Kinematics

3.1.1 Gas morphology and kinematics

Rawat et al. (2023), based on ^{12}CO spectrum and comparing the CO gas morphology with the dust continuum images (*Herschel* images at 250, 350 and 500 μm), showed that the G148.24+00.41 cloud component mainly lies in the velocity range of -37.0 km s $^{-1}$ to -30.0 km s $^{-1}$ in agreement with the previous studies (e.g. Urquhart et al. 2008; Miville-Deschênes et al. 2017). Fig. 2 shows the average spectrum of all three isotopologues towards the cloud. We fitted a Gaussian function to the line profiles and derived the peak velocity, velocity dispersion (σ_{1d}), and velocity range of each spectrum, which are given in Table 1. The estimated line-width ($\Delta V = 2.35 \sigma_{1d}$) and 3D velocity dispersion ($\sigma_{3d} = \sqrt{3} \times \sigma_{1d}$) associated with the ^{12}CO profile are 3.55 and 2.62 km s $^{-1}$, for ^{13}CO are 2.30 and 1.70 km s $^{-1}$, and for C^{18}O are 2.04 and 1.51 km s $^{-1}$, respectively. We want to point out that the optical thickness of ^{12}CO may affect the velocity centroid and velocity dispersion of the line profile. Therefore, the ^{12}CO data has been used to measure the global properties and distribution of low-density gas, while the kinematics of dense structures or properties of dense clumps have been derived using the ^{13}CO and C^{18}O data.

The integrated intensity (moment-0) maps of ^{12}CO , ^{13}CO , and C^{18}O line emissions, integrated in the velocity range given in Table 1, are shown in Fig. 3. Also shown are the contours above 3σ of the background value, where σ is the standard deviation of the background emission. As discussed earlier, in molecular clouds, the ^{12}CO traces better the diffuse emission, while ^{13}CO and C^{18}O probe deeper into the cloud and trace higher column density regions. Though the spatial resolution of the data is relatively low, the presence of several filamentary structures can be seen in the ^{13}CO map (details are discussed in section 3.2), while C^{18}O emission seems better at tracing the central area and the dense clumpy structures of the cloud. In G148.24+00.41, we find that ^{13}CO covers $\sim 87\%$ of the ^{12}CO emission, while C^{18}O covers only 43%.

In order to understand the overall velocity distribution and velocity dispersion of the ^{12}CO and ^{13}CO gas in the cloud, we made intensity-weighted mean velocity (moment-1) and velocity dispersion (moment-2) maps, which are shown in Figs. 4a-b and Figs. 4c-d, respectively. In general, the velocity distribution maps reveal that the outer extent of the cloud exhibits blue-shifted velocities relative to the systematic one, typically ranging from -36 to -34 km s $^{-1}$, while the central region displays a red-shifted velocity range, from -34 to -30 km s $^{-1}$. We note that, since moment analysis represents the mean velocity of the gas along the line of sight, it is insensitive to the kinematics of the multiple velocity structures, if present in the cloud (more discussion in Section 3.2.2). Figs. 4c-d shows that the velocity dispersion is not uniform across G148.24+00.41, it varies from 0.2 to 2.3 km s $^{-1}$, with a notable increase in the cloud's central area. The velocity dispersion of ^{12}CO gas may be on the higher side due to the optical depth effect, but this trend also holds true for the relatively optically thin ^{13}CO line. In the central area, a patchy increase in velocity dispersion can be seen at several locations. We discuss more on this in Section 3.3.2. Additionally, the ^{12}CO map reveals high velocity dispersion in the north-eastern side of the cloud, whose exact reason is not known to us. External shock compression can result in such high dispersions. Although a young (~ 4 Myr) H II region is found to be present in the vicinity of the cloud (Romero &

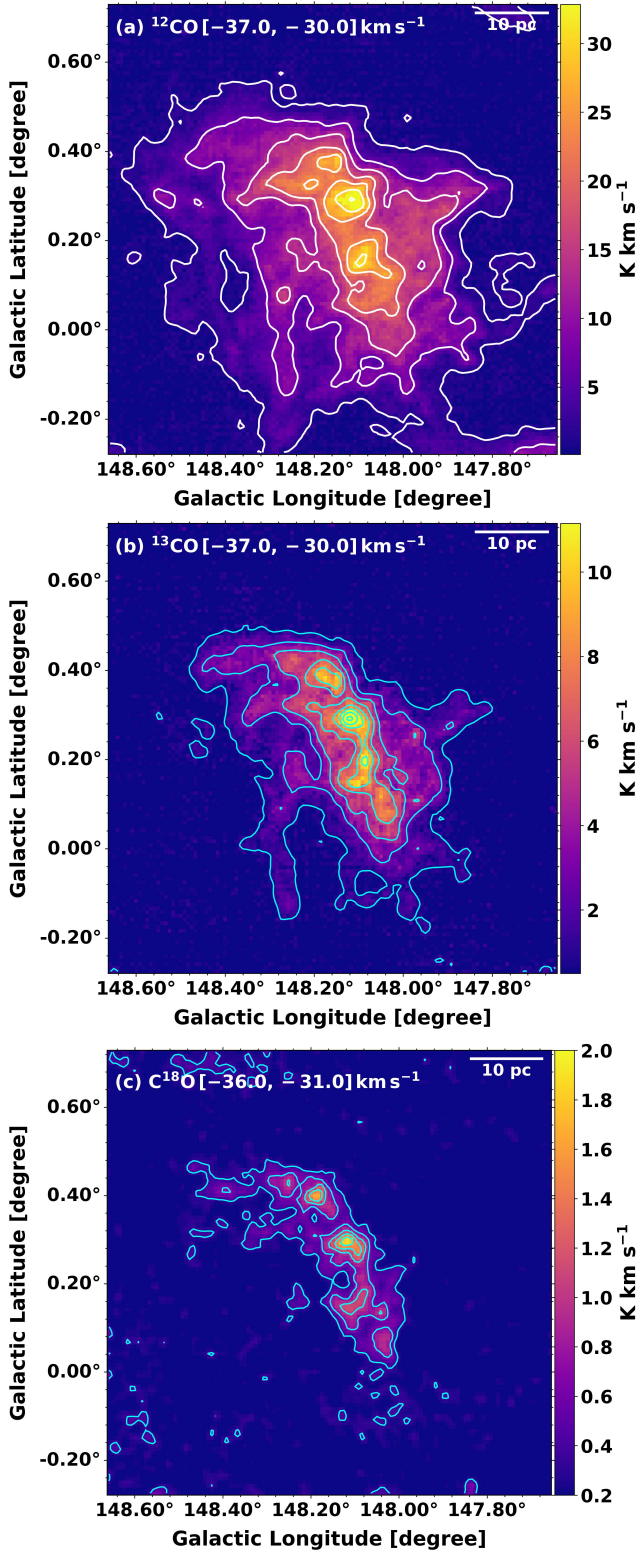


Figure 3. (a) ^{12}CO integrated intensity (moment-0) map of the cloud with contour levels at 1.5, 7.08, 12.67, 18.25, 23.83, 29.42, and 35 K km s^{-1} . (b) ^{13}CO integrated intensity map of the cloud with contour levels at 0.9, 2.7, 4.5, 6.3, 8.1, 9.9, 11.7, and 13.5 K km s^{-1} . (c) C^{18}O integrated intensity map of the cloud with contour levels at 0.35, 0.68, 1.01, 1.34, 1.67, and 2.0 K km s^{-1} . The contours are drawn 3σ above the background value of individual maps. We note that the C^{18}O map has been smoothed by 1 pixel to improve the signal.

Cappa 2009). However, the H II region is located in the south-western direction of G148.24+00.41 and is also at a different distance (i.e. ~ 1 kpc) with respect to it. A detailed investigation covering wider surroundings of G148.24+00.41 is needed to better understand its origin, which is beyond the scope of the present work.

3.1.2 Physical conditions and gas column density

Assuming the molecular cloud is under the local thermodynamic equilibrium (LTE) and ^{12}CO is optically thick, the excitation temperature (T_{ex}), optical depth (τ), and column density ($N(\text{H}_2)$) of the G148.24+00.41 cloud can be calculated with the measured brightness of CO isotopologues. Under LTE, the kinetic temperature of the gas is assumed to correspond to the excitation temperature.

The brightness temperature under the Rayleigh-Jeans approximation is expressed as $T_{\text{MB}} = f \times [J(T_{\text{ex}}) - J(T_{\text{bg}})](1 - e^{-\tau})$, where T_{MB} is the brightness temperature, f is the beam filling factor, T_{bg} is the cosmic microwave background temperature, and $J(T) = \frac{h\nu}{k(\exp(h\nu/kT) - 1)}$. Taking $T_{\text{bg}} \sim 2.7$ K and assuming $f=1$, T_{ex} can be derived and written in a simplified form (Garden et al. 1991; Nishimura et al. 2015; Xu et al. 2018) as :

$$T_{\text{ex}}^{12,1-0} = \frac{5.53}{\ln \left[1 + \frac{5.53}{T_{\text{MB,peak}}^{12,1-0} + 0.84} \right]}, \quad (1)$$

where $T_{\text{MB,peak}}^{12,1-0}$ is the peak brightness temperature of the ^{12}CO emission along the line of sight. Based on the above formalism, we derived the excitation temperature at each pixel of the cloud. Fig. 5a shows the excitation temperature map, which ranges from 5 K to 21 K with a median around 8 K. The temperature map shows a relatively high temperature in the central region of the cloud with respect to the outer extent. This is likely due to the fact that the central region is heated by the protostellar radiation, where it has been found that protostars are actively forming (Rawat et al. 2023). The obtained average excitation temperature of the cloud is found to be similar to the ^{12}CO based excitation temperature of massive GMCs with embedded filamentary dark clouds (e.g. ~ 7.4 K, Hernandez & Tan 2015, and references therein) and also similar to other nearby molecular clouds such as Taurus (~ 7.5 K, Goldsmith et al. 2008) and Perseus (~ 11 K, Pineda et al. 2008).

Next we derived the optical depth maps of ^{13}CO and C^{18}O gas using the following relations (Garden et al. 1991; Pineda et al. 2010):

$$\tau_{13} = -\ln \left[1 - \frac{T_{\text{MB,peak}}^{13}}{5.29} \left[\frac{1}{\exp(5.29/T_{\text{ex}}) - 1} - 0.164 \right]^{-1} \right] \quad (2)$$

$$\tau_{18} = -\ln \left[1 - \frac{T_{\text{MB,peak}}^{18}}{5.27} \left[\frac{1}{\exp(5.27/T_{\text{ex}}) - 1} - 0.166 \right]^{-1} \right], \quad (3)$$

where $T_{\text{MB,peak}}^{13}$ and $T_{\text{MB,peak}}^{18}$ is the peak brightness temperature of ^{13}CO and C^{18}O , respectively.

The optical depths of ^{13}CO and C^{18}O lines are estimated to be $0.1 < \tau(^{13}\text{CO}) < 3.0$ and $0.05 < \tau(\text{C}^{18}\text{O}) < 0.25$, respectively. Fig. 5b shows the optical depth map of the ^{13}CO emission. Within the cloud area, we found only a 5% fraction of the cloud area is of high ($\tau > 1$) optical depth, implying that most of the observed ^{13}CO emission is optically thin.

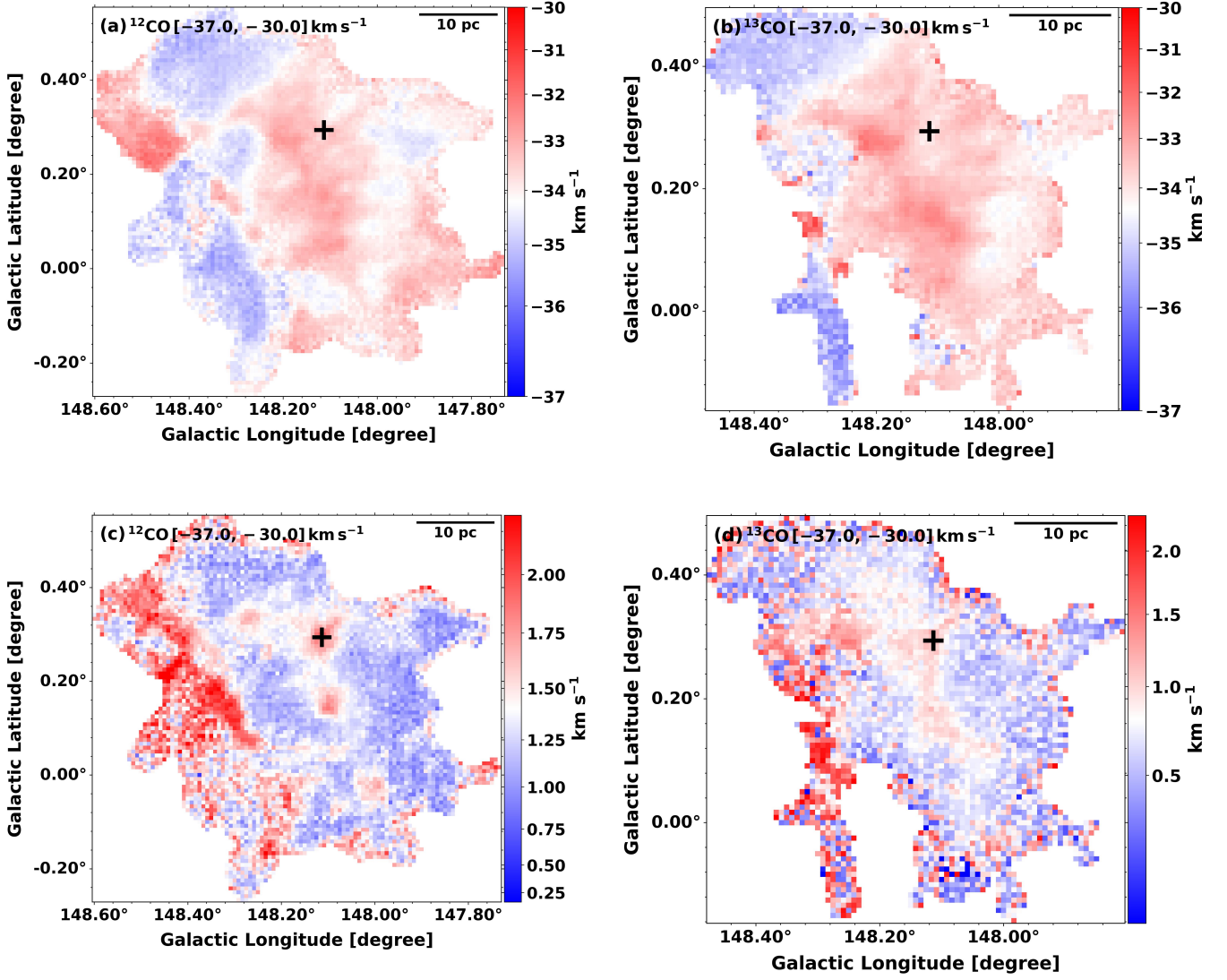


Figure 4. (a) ^{12}CO and (b) ^{13}CO velocity maps of G148.24+00.41. (c) ^{12}CO and (d) ^{13}CO velocity dispersion maps of G148.24+00.41. The location of the hub is marked with a plus sign.

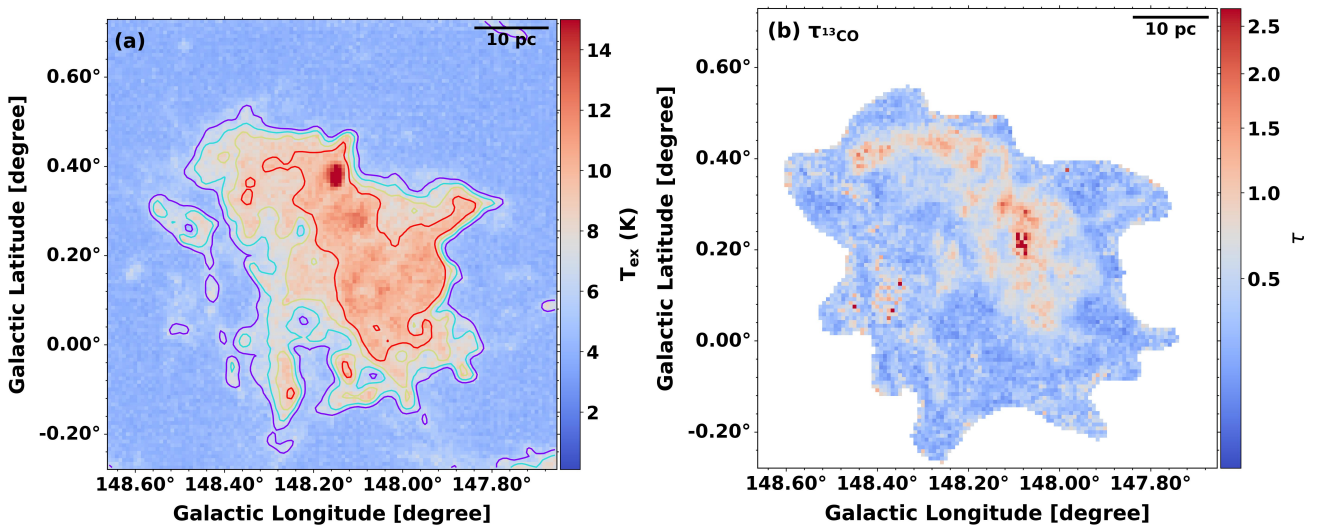


Figure 5. (a) Excitation temperature map overplotted with contours at 6, 7, 8, and 9 K. (b) Optical depth map of ^{13}CO .

We then obtained the column density of ^{13}CO and C^{18}O using the following relations from Bourke et al. (1997):

$$N(^{13}\text{CO})_{\text{thin}} = 2.42 \times 10^{14} \times \left(\frac{T_{\text{ex}} + 0.88}{1 - \exp(-5.29/T_{\text{ex}})} \right) \times \frac{1}{J(T_{\text{ex}}) - J(T_{\text{bg}})} \int T_{\text{MB}}(^{13}\text{CO}) dv \quad (4)$$

$$N(\text{C}^{18}\text{O})_{\text{thin}} = 2.42 \times 10^{14} \times \left(\frac{T_{\text{ex}} + 0.88}{1 - \exp(-5.27/T_{\text{ex}})} \right) \times \frac{1}{J(T_{\text{ex}}) - J(T_{\text{bg}})} \int T_{\text{MB}}(\text{C}^{18}\text{O}) dv \quad (5)$$

However, the ^{13}CO based column density may underestimate the column density in the central area of the cloud, where ^{13}CO is optically thick. Many studies on the GMCs and Infrared Dark Clouds have accounted for line optical depth while estimating their physical properties (Roman-Duval et al. 2010; Hernandez et al. 2011). We, thus applied the following correction to the $N(^{13}\text{CO})_{\text{thin}}$ following Pineda et al. (2010); Li et al. (2015). Since the observed C^{18}O emission is optically thin, no optical depth correction was made to $N(\text{C}^{18}\text{O})_{\text{thin}}$.

$$N(^{13}\text{CO})_{\text{corrected}} = N(^{13}\text{CO})_{\text{thin}} \times \frac{\tau_{13}}{1 - e^{-\tau_{13}}} \quad (6)$$

We then convert the ^{13}CO and C^{18}O column density to the molecular hydrogen column density ($N(\text{H}_2)$) using the relation, $N(\text{H}_2) = 7 \times 10^5 N(^{13}\text{CO})$ (Frerking et al. 1982) and $N(\text{H}_2) = 7 \times 10^6 N(\text{C}^{18}\text{O})$ (Castets & Langer 1995), respectively. The molecular hydrogen column densities from the ^{13}CO and C^{18}O gas emission are estimated to be around $0.9 \times 10^{21} \text{ cm}^{-2} < N(\text{H}_2)_{^{13}\text{CO}} < 2.4 \times 10^{22} \text{ cm}^{-2}$ and $1.1 \times 10^{21} \text{ cm}^{-2} < N(\text{H}_2)_{\text{C}^{18}\text{O}} < 2.0 \times 10^{22} \text{ cm}^{-2}$, respectively. We found for the common area, the column density of both the maps are in agreement with each other by a factor of 1.5. The observed variation in column density values might be due to the abundance variations of these isotopologues. For example, chemical models and observations suggest that selective photo-dissociation and fractionation can significantly affect the abundance of CO isotopologues (e.g. Shimajiri et al. 2015; Liszt 2017).

Since ^{13}CO covers a larger area and has a better signal-to-noise ratio compared to C^{18}O , thus, we used ^{13}CO based column density map for further analysis, such as in deriving the global properties of the cloud. Fig. 6 shows the ^{13}CO based $N(\text{H}_2)$ map, tracing well the central dense location of the cloud. We find the peak value of $N(\text{H}_2)$ is around $2.4 \times 10^{22} \text{ cm}^{-2}$, which corresponds to the location of the hub.

The ^{12}CO emission in G148.24+00.41 is more extended than ^{13}CO emission; thus, for estimating column density of the cloud area located outside the boundary of ^{13}CO emission, we also estimated the hydrogen column density of each pixel directly from the ^{12}CO intensity, $I(^{12}\text{CO})$. To do so, we use the relation $N(\text{H}_2) = X_{\text{CO}} I(^{12}\text{CO})$, where X_{CO} is the CO-to- H_2 conversion factor, whose typical value is $\sim 2.0 \times 10^{20} \text{ cm}^{-2} (\text{K km s}^{-1})^{-1}$ (Dame et al. 2001; Bolatto et al. 2013; Lewis et al. 2022) with an uncertainty of around 30% (Bolatto et al. 2013). We also estimated the total ^{12}CO column density from the ^{13}CO optical depth map, using an average value of $^{12}\text{CO} / ^{13}\text{CO}$ abundance of ~ 60 (Frerking et al. 1982) and equation 3 of Garden et al. (1991). Doing so, we found that the total molecular

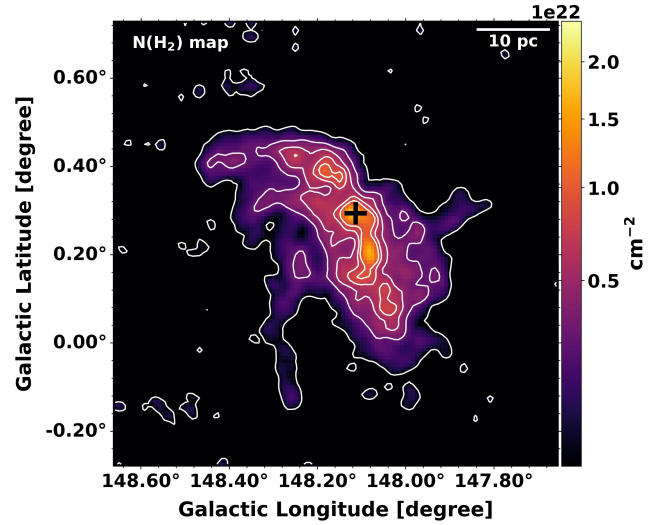


Figure 6. $N(\text{H}_2)$ column density map based on ^{13}CO . The contour levels are shown above 3σ of the background value, starting from 0.9×10^{21} to $9 \times 10^{21} \text{ cm}^{-2}$. The location of the hub is marked with a plus sign.

hydrogen column density of the cloud based on both approaches is within a factor of 1.3.

We then combined ^{12}CO and ^{13}CO column density maps to make a composite molecular hydrogen column density map. For the area lying outside the area of ^{13}CO emission, we take the column density values from the ^{12}CO emission. Although we use $N(\text{H}_2)_{^{13}\text{CO}}$ column density values within the ^{13}CO emission area, we observed that some of the pixels in the central area of the ^{13}CO map exhibit lower column density values than the neighbouring pixels. Overall, these outliers do not affect the measured global properties. Nonetheless, in these pixels, if the ratio (R) of $N(\text{H}_2)_{^{13}\text{CO}}$ to $N(\text{H}_2)_{^{12}\text{CO}}$ is found to be > 1 , the pixel values from the $N(\text{H}_2)_{^{13}\text{CO}}$ map are considered, otherwise, from the $N(\text{H}_2)_{^{12}\text{CO}}$ map. The combined composite map made in this way is shown in Fig. 7. The column density of the composite map lies in the range of $0.2 \times 10^{21} \text{ cm}^{-2}$ to $2.4 \times 10^{22} \text{ cm}^{-2}$. We checked the difference in column density values at the boundary of ^{13}CO emission from both the tracers and found that they are within a factor of 1.2, thus reasonably agreeing with each other.

3.1.3 Global cloud properties and comparison with Galactic clouds

We obtained the cloud properties like mass, effective radius, surface density, and volume density, following the approach described in Rawat et al. (2023). Briefly, we estimated the mass of the cloud using the relation.

$$M_c = \mu_{\text{H}_2} m_{\text{H}} A_{\text{pixel}} \Sigma N(\text{H}_2), \quad (7)$$

where m_{H} is the mass of hydrogen, A_{pixel} is the area of a pixel in cm^2 , and μ_{H_2} is the mean molecular weight that is assumed to be 2.8 (Kauffmann et al. 2008). We define the outer extent (thus the area) of G148.24+00.41 for different tracers by considering emission within the 3σ contours (see Fig. 3) and derive its properties within this area. The cloud mass from ^{12}CO , ^{13}CO , and C^{18}O based $N(\text{H}_2)$ column density map, calculated above the 3σ emission is $\sim 5.8 \times 10^4 M_{\odot}$, $\sim 5.6 \times 10^4 M_{\odot}$, and $\sim 3.5 \times 10^4 M_{\odot}$, respectively. The cloud mass estimated from the composite column density map is found to be $\sim 7.2 \times 10^4 M_{\odot}$. To check the boundness status

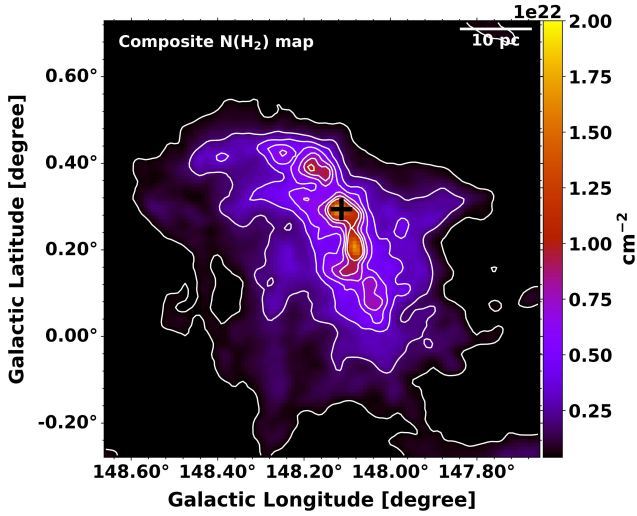


Figure 7. Composite column density map made based on ^{12}CO and ^{13}CO column density maps. The contour levels are shown above 3σ of the background value, starting from 4.3×10^{20} to $1 \times 10^{22} \text{ cm}^{-2}$. The location of the hub is marked with a plus sign.

of G148.24+00.41, we calculated its virial mass using the relation, $M_{\text{vir}} = 126 \times 1.33 r_{\text{eff}} \Delta V^2$, for density index, $\beta = 1.5$ (see Eqn. 2 of Rawat et al. 2023). Using r_{eff} and ΔV values of ^{12}CO , ^{13}CO , and C^{18}O (see Table 1), the estimated M_{vir} is around $\sim 4 \times 10^4 M_{\odot}$, $1.5 \times 10^4 M_{\odot}$, and $8.6 \times 10^3 M_{\odot}$, respectively. Since the virial mass of G148.24+00.41, as estimated by ^{12}CO , ^{13}CO , and C^{18}O , is less than their respective gas mass, it implies that the cloud is bound in all three CO isotopologues. We acknowledge that the optical thickness of ^{12}CO line can make the line profile broader, as discussed in Section 3.1.1, thus, the ^{12}CO based virial mass can be an upper limit. Even then, the aforementioned boundness status of the cloud will remain true.

The typical uncertainty associated with the estimation of gas mass from the ^{12}CO , ^{13}CO , and C^{18}O emissions is in the range 35–44%. Because the uncertainty in the assumed X_{CO} factor and in the isotopic abundance values of CO molecules, used in converting $N(\text{CO})$ to $N(\text{H}_2)$ is around 30 to 40% (Wilson & Rood 1994; Savage et al. 2002; Bolatto et al. 2013). The distance uncertainty associated to the cloud is around 9%. In addition, the estimation of $N(\text{CO})$ is also affected by the uncertainty associated with the estimated gas kinematic temperature. In the present case, we find that the average gas kinetic temperature (8 K) is lower than the average dust temperature of the cloud, $14.5 \pm 2 \text{ K}$ (Rawat et al. 2023). When gas and dust are well mixed, the gas kinematic temperature better corresponds to the dust temperature, and this occurs when the density is $> 10^4 \text{ cm}^{-3}$. For example, Goldsmith (2001) found that dust and gas are better coupled at volume densities above 10^5 cm^{-3} , which are typically not traced by ^{12}CO and ^{13}CO data ($n_{\text{crit}} < 10^4 \text{ cm}^{-3}$). They find a temperature difference of $\sim 4 \text{ K}$ at density $\sim 10^5 \text{ cm}^{-3}$ and completely negligible at density $\sim 10^6 \text{ cm}^{-3}$. Moreover, it is also suggested that if the volume density of the gas is lower than the critical density of ^{12}CO , this would lead to a lower excitation temperature (Heyer et al. 2009). Assuming the true average temperature of the gas is around 14 K, we estimated that it would change the ^{13}CO column density by a factor of 14%, hence the estimated gas mass would also change by this factor.

In the present work, though we have derived the masses using canonical values of X factor and the CO abundances, however, it is

worth mentioning that many studies have suggested that these values increase towards the outer galaxy (Nakanishi & Sofue 2006; Pineda et al. 2013; Heyer & Dame 2015; Patra et al. 2022). Since G148.24+00.41 is located in the outer galaxy (i.e. $\sim 11.2 \text{ kpc}$ from the Galactic centre), the derived masses are likely underestimations. For example, we find that implementing X_{CO} value from the relation given in Nakanishi & Sofue (2006), would increase the total $N(\text{H}_2)_{^{12}\text{CO}}$ column density and thus, the mass by a factor of ~ 2 .

The total gas mass estimated for G148.24+00.41 in the present work using the composite column density map, within uncertainty, agrees with the dust-based gas mass $\sim (1.1 \pm 0.5) \times 10^5 M_{\odot}$, derived by Rawat et al. (2023). In Table 1, we have tabulated the cloud mass, mean column density, effective radius, surface density, and volume density of the cloud. The derived surface mass density from ^{12}CO , ^{13}CO , C^{18}O , and composite map is $\sim 52, 59, 72$, and $63 M_{\odot} \text{ pc}^{-2}$, respectively. The surface mass density from ^{12}CO is similar to the value which we have obtained for G148.24+00.41 from the dust continuum and dust extinction-based column density maps for the same area, (i.e. $\Sigma_{\text{gas}} = 54 M_{\odot} \text{ pc}^{-2}$, see Rawat et al. 2023). Since the isotopologues trace different areas of the cloud, their estimated surface densities are different, with a gradual increase from low-density to high-density tracer.

Comparing the properties of G148.24+00.41 with other Galactic clouds, we find that the ^{12}CO surface density of G148.24+00.41 is significantly higher than the average surface density ($\sim 10 M_{\odot} \text{ pc}^{-2}$) of the outer Galaxy molecular clouds of our own Milkyway (Miville-Deschênes et al. 2017). Miville-Deschênes et al. (2017) studied Galactic plane clouds using ^{12}CO and found that the average mass surface density of clouds is higher in the inner Galaxy, with a mean value of $41.9 M_{\odot} \text{ pc}^{-2}$, compared to $10.4 M_{\odot} \text{ pc}^{-2}$ in the outer Galaxy. Similarly, we also find that the derived ^{13}CO surface density of G148.24+00.41 is on the higher side of the surface densities of the Milkyway GMCs studied by Heyer et al. (2009). Heyer et al. (2009) found an average surface density value $\sim 42 M_{\odot} \text{ pc}^{-2}$ using ^{13}CO data, assuming LTE conditions and a constant H_2 to ^{13}CO abundance, similar to the approach used in this work. Recently Lewis et al. (2022) investigated nearby star or star-cluster forming GMCs, including Orion-A, using ^{12}CO emission and similar X_{CO} factor used in this work. Comparing the surface densities of these clouds, we find that the surface density of G148.24+00.41 is higher than most of their studied GMCs (average $\sim 37.3 \pm 10 M_{\odot} \text{ pc}^{-2}$) and comparable to the surface density of Orion-A (see Fig. 8 of Lewis et al. 2022). All the aforementioned comparisons support the inference drawn by Rawat et al. (2023) on G148.24+00.41 based on the dust continuum analysis, i.e. G148.24+00.41 is indeed a massive GMC like Orion-A.

3.2 Filaments and Filamentary Structures

As mentioned in Section 1, based on dust continuum maps, Rawat et al. (2023) suggested that the central cloud region likely consists of six filaments, forming a hub filamentary system (HFS) with the hub being located at the nexus or junction of these filaments. Molecular clouds with HFSs are of particular interest because these are the sites where cluster formation would take place, as advocated in many simulations (e.g. Naranjo-Romero et al. 2012; Gómez & Vázquez-Semadeni 2014; Gómez et al. 2018; Vázquez-Semadeni et al. 2019). Massive and elongated hub regions are sometimes referred to as “ridges” (e.g. Hennemann et al. 2012; Tigé et al. 2017; Motte et al. 2018).

The line-of-sight (LOS) velocity gradient, traced by molecular

Table 1. G148.24+00.41 properties from CO emission. The mass of the cloud from ^{12}CO , ^{13}CO , and C^{18}O is calculated above 3σ from the mean background emission. The FWHM is the line-width of the spectra, calculated as $\Delta V = 2.35\sigma_{1D}$.

Emission	Velocity interval (km s^{-1})	V_{peak} (km s^{-1})	FWHM (ΔV) (km s^{-1})	Mean $N(\text{H}_2)$ ($\times 10^{21} \text{ cm}^{-2}$)	Mass (M_{\odot})	$n(\text{H}_2)$ (cm^{-3})	r_{eff} (pc)	Σ_{gas} ($M_{\odot} \text{ pc}^{-2}$)
^{12}CO	(−37.0, −30.0)	−34.07	3.55	2.3	5.8×10^4	30	18.8	52
^{13}CO	(−37.0, −30.0)	−33.83	2.30	2.6	5.6×10^4	37	17.3	59
C^{18}O	(−36.0, −31.0)	−33.72	2.04	3.2	3.5×10^4	63	12.4	72
Composite-map (^{12}CO & ^{13}CO)	(−37.0, −30.0)	—	—	2.8	7.2×10^4	37	19.0	63

lines, is commonly interpreted as a proxy for the plane-of-sky (POS) gas motion. Recent molecular line observations have revealed the kinematic structures of several HFSs in nearby clouds, and significant velocity gradients are observed along several filaments that are attached to HFSs (e.g. Liu et al. 2012; Friesen et al. 2013; Hacar et al. 2018; Dewangan et al. 2020; Chen et al. 2020; Yang et al. 2023; Liu et al. 2023). These gas motions are thought to represent dynamical gas flows which are fuelling the hub. In the following, we identify and characterize the filamentary structures in the cloud and discuss their role in star and cluster formation observed in the cloud.

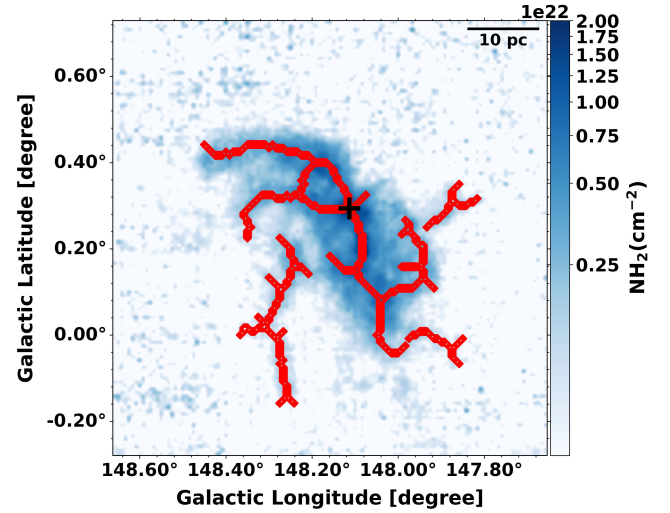
3.2.1 Identification of global filamentary structures

We used a python-based package - *FilFinder*¹ (Koch & Rosolowsky 2015) to identify the filamentary structures of the cloud (details of *FilFinder* is given in Appendix A) using the ^{13}CO based molecular hydrogen column density map. Fig. 8 shows the extracted skeletons of the G148.24+00.41 cloud. It can be seen that the *Filfinder* algorithm reveals several filamentary structures, including the main central filament that runs from north-east to south-west, and also several nodes where the filaments are intersecting.

The column density map is created from the integrated intensity map. So it's important to acknowledge that in the integrated intensity map, multiple individual velocity features may blend together and appear as a single one, as observed in nearby filamentary clouds (e.g. Hacar et al. 2013, 2017) or in distant ridge (e.g. Hu et al. 2021; Cao et al. 2022). Velocity sub-structures of gas in a cloud can be inspected using channel maps, in which the emission integrated over a narrow velocity range is examined. It is then possible to identify individual velocity coherent structures that are very likely to correspond to the physically distinct structures of the cloud.

3.2.2 Small-scale gas motion and velocity coherent structures

Fig. 9 shows the ^{13}CO velocity channel maps with a step of 0.34 km s^{-1} . As can be seen from the channel maps, along with several compact emissions, multiple spatially elongated velocity structures are also present. These elongated structures are marked as St-1, St-2, St-3, St-4, St-5, and St-6 on the map. The location of these structures in the map corresponds to either the maximum intensity feature or has relatively the longest distinct visible structure, or both. These structures have noticeable differences in velocity because they emerge in different velocity channels.

**Figure 8.** Global skeletons of G148.24+00.41 showing the filamentary structures, main ridge, nodes, and central hub location, over the ^{13}CO based $N(\text{H}_2)$ map. The location of the hub is marked with a plus sign.

The majority of these structures appear to move towards the hub location, marked by a plus sign on the map. The merger and convergence of these structures form a nearly continuous structure in the central area of the cloud that we refer to as the "ridge" in which the hub is located. The ridge is marked by a solid green line on the channel map. The ridge also seems to be attached to several small-scale strand-like, nearly perpendicular elongated structures (shown by arrows in Fig. 9). The kinematic association of such perpendicular structures with the main filament/ridge indicates the possible direct role of the surrounding gas on the formation and growth of the main filament/ridge (e.g. Cox et al. 2016). Besides, one can see that the structure, St-2, is composed of 2-3 small-scale filamentary structures that are seen in the channel maps at around -35.1 to -34.4 km s^{-1} . These structures are indistinguishable in the integrated intensity map shown in Fig. 3b, emphasizing that some of the elongated filamentary structures that we are seeing in the integrated intensity map could be the sum of multiple velocity coherent structures.

3.2.3 Likely velocity coherent filaments

In molecular clouds, small-scale velocity coherent filaments (VCF) have been identified using position-position-velocity (PPV) maps, where the velocity components are grouped based on how closely

¹ <https://github.com/e-koch/FilFinder>

they are linked in both position and velocity simultaneously (e.g. [Hacar et al. 2013](#)). In the literature, identification of VCFs is primarily done using high-resolution and high-density tracer (e.g. NH_3 , N_2H^+ , C^{18}O) data cubes and preferentially on the nearby clouds, where structures are well resolved (e.g. [Hacar et al. 2017, 2018](#); [Shimajiri et al. 2019](#)). However, as witnessed from the channel maps, the gas kinematics of the cloud is quite complicated with overlapping structures. Disentangling and identifying individual velocity coherent structures is challenging with the present data. None the less, to identify the likely VCF of G148.24+00.41, we followed an approach similar to that of the nearby molecular clouds. We visually inspected the ^{13}CO data cube and identified the velocity coherent structures that are continuous in position as well as velocity in the data cube. We then made the integrated intensity map of the structure by integrating the emission in the velocity range that encompasses the majority of its emission. In this way, we identified six likely velocity coherent filamentary structures in G148.24+00.41.

Fig. 10 shows an example of an intensity map, integrated in the sub-velocity range, $[-37.0, -34.0] \text{ km s}^{-1}$, where filament F1, F2, and F3 are identified, while F4, F5 and F6, are identified in the full velocity integrated intensity map (see Fig. 8). Compared to Fig. 10, the identification and delineation of F3 filament is confusing and difficult in Fig. 8, whereas in Fig. 10, the structure of F3 is better apparent, and seems to connect to F2. We note that although our approach is subject to the choice of velocity range, we find that except for one, the majority of the identified structures matched well with the structures shown in Fig. 8, but separated into different velocity coherent filaments.

All the identified structures are marked in Fig. 11 as F1, F2, F3, F4, F5, and F6. Most of these filaments correspond to the structures marked in Figure 9. The length of the filaments lies in the range of 15–40 pc. It is important to emphasize that while we have identified six probable filaments within the cloud based on our data, we acknowledge that the identification of such structures is also subject to the resolution of the data. Comparing the morphology of the ^{13}CO integrated intensity based filamentary structures identified here with the dust-based filamentary structures visually identified by [Rawat et al. \(2023\)](#) in the central region of the cloud, we find that the filaments F2, F5, and F6 reasonably agree with the major filaments of [Rawat et al. \(2023\)](#) marked in Fig. 1. While the smaller *Herschel* filaments attached to the hub are not identifiable in our low-resolution data. Future high-resolution observations may resolve the filaments into multiple sub-filaments (e.g. [Hu et al. 2021](#)). We proceed with the present available data to characterize the identified filamentary structures to get a sense of their role in the cluster formation of the cloud.

3.2.4 Properties of the filaments

We make use of *RadFil*² ([Zucker & Chen 2018](#)), a python-based tool to obtain the radial profile and width of the filament. *RadFil* also uses the *FilFinder* to generate the filament spines. It requires two inputs, image data, and filament mask, which we provided from the output of *FilFinder* for the individual filament. Fig. 11 shows the extracted filament spines over their ^{13}CO integrated intensity emission. *RadFil* makes radial profiles of perpendicular cuts drawn along the filament spine as shown in Fig. 12a for filament F2 and then obtains filament width (Full Width Half Maxima, FWHM) by fitting a Gaussian function considering all the radial profiles (the detailed

description of the procedures is given in Appendix B) as shown in Fig. 12b.

We obtained the deconvolved FWHM by taking into account the beam size ($52''$) as:

$$\text{FWHM}_{\text{decon}} = \sqrt{\text{FWHM}^2 - \text{FWHM}_{\text{bm}}^2} \quad (\text{Könyves et al. 2015}),$$
 where FWHM_{bm} is the beam size. The obtained $\text{FWHM}_{\text{decon}}$ for all the filaments are listed in Table 2.

In our case, the filament widths turn out to be in the range of 2.5–4.2 pc, with a mean ~ 3.7 pc. The obtained widths are found to be higher than the typical width of ~ 0.1 pc obtained from *Herschel*-based dust emission analysis of nearby clouds (e.g. [André et al. 2010, 2014](#); [Arzoumanian et al. 2019](#)). However, it is worth noting that many observations and simulations have also argued that the width of filaments depends on many factors such as the fitted area, used tracer, resolution of the data, distance, evolutionary status of the filaments, and magnetic field (e.g. see [Smith et al. 2014](#); [Schisano et al. 2014](#); [Federrath 2016](#); [Panopoulou et al. 2017](#); [Suri et al. 2019](#); [Panopoulou et al. 2022](#)). For example, [Panopoulou et al. \(2022\)](#) found that the mean filament width for the nearby clouds is different from that of far away clouds. They also found that the mean per cloud filament width scales with the distance approximately as 4–5 times the beam size. Although the debate on the characteristic filament width of 0.1 pc is yet to be settled (see discussion in [Panopoulou et al. 2017, 2022](#)); we want to emphasize that our extracted filament widths might be on the higher side because G148.24+00.41 is located at a distance of ~ 3.4 kpc and analysed with the low-resolution (~ 0.9 pc) and low-density tracer CO data. Moreover, some of the filaments (e.g. F2) could be the sum of a series of sub-filaments, whereas filaments in nearby clouds are well resolved. In addition, ^{13}CO is tracing better the enveloping layer of the filaments. None the less, it is worth mentioning that using the PMO ^{13}CO data, [Liu et al. \(2021\)](#) and [Guo et al. \(2022\)](#), found similar mean filament widths of ~ 3.8 pc and ~ 2.9 pc, respectively, for Galactic plane filamentary clouds located at 2.4 kpc and 4.5 kpc, respectively.

Future, high-resolution molecular data may be able to better characterize the filaments of G148.24+00.41. However, with the available data, we proceed to derive the properties of the filaments, such as mean line mass and column density, as well as the kinematics and dynamics of the filaments along their spines.

We estimated the total mass of the filaments within their widths using the same procedure discussed in Section 3.3.2, and then divide the mass by the length of the filaments to obtain mass per unit length, M_{line} , of the filaments. The properties of the filament, such as total mass, mean $\text{N}(\text{H}_2)$, aspect ratio (i.e. length/width), and M_{line} are tabulated in Table 2. The aspect ratios of the filaments are in the range of 4–10. Generally, a filament is characterized by an elongated structure with an aspect ratio greater than ~ 3 –5 ([André et al. 2014](#)). The M_{line} of the filaments F1, F2, F3, F4, F5, and F6 is found to be 92, 171, 93, 138, 233, and 396 $\text{M}_{\odot} \text{ pc}^{-1}$, respectively, with a mean around 187 $\text{M}_{\odot} \text{ pc}^{-1}$. M_{line} is a critical parameter for assessing the dynamical stability of the filaments, which we discuss in Section 4.1.

3.2.5 Kinematics and dynamics of the gas along the spine

To examine the kinematics, physical conditions, and dynamics of the gas along the filaments, we used ^{13}CO molecular line data and estimated the parameters within the filament width. In Fig. 13, we show the variation of velocity, velocity dispersion, column density, and excitation temperature along the filament spines from their tail to head. We refer to the tail as the farthest point of the filament spine

² <https://github.com/catherinezucker/radfil>

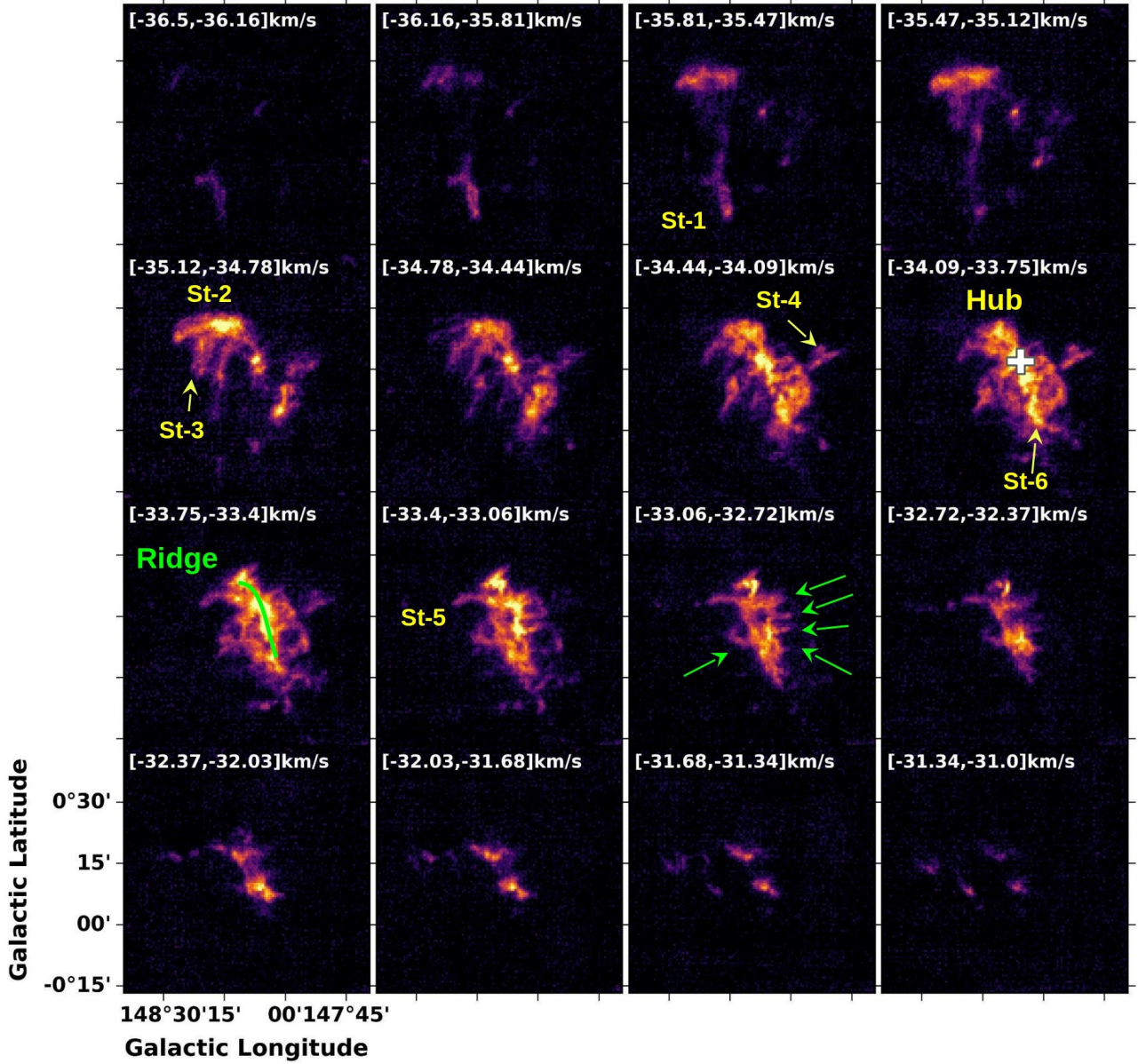


Figure 9. Velocity channel maps in units of K km s^{-1} for the ^{13}CO emission. The velocity ranges of the channel maps are indicated at the top left of each panel. The ridge (green curve), strands (green arrows), structures (yellow arrows), and the hub location (plus) are marked in the channel maps.

Table 2. Filament properties determined from ^{13}CO . The filament F1, F2, and F3 are extracted in the velocity range, $[-37.0, -34.0] \text{ km s}^{-1}$, while the filament F4, F5, and F6 are extracted in the velocity range, $[-37.0, -30.0] \text{ km s}^{-1}$.

Filament	Length (pc)	Width (pc)	Mass ($\times 10^3 M_{\odot}$)	Mass _{line} ($M_{\odot} \text{ pc}^{-1}$)	Mass _{crit} ($M_{\odot} \text{ pc}^{-1}$)	Mean $\text{N}(\text{H}_2)$ ($\times 10^{21} \text{ cm}^{-2}$)	$\frac{\sigma_{\text{nl}}}{c_s}$
F1	38.0	3.61	3.5	92	90	1.1	2.4
F2	25.7	4.16	4.4	171	94	3.0	2.4
F3	14.0	3.53	1.3	93	90	1.5	2.4
F4	18.1	3.28	2.5	138	215	2.3	3.7
F5	14.6	2.69	3.4	233	495	4.4	5.8
F6	17.4	2.49	6.9	396	283	9.0	4.0

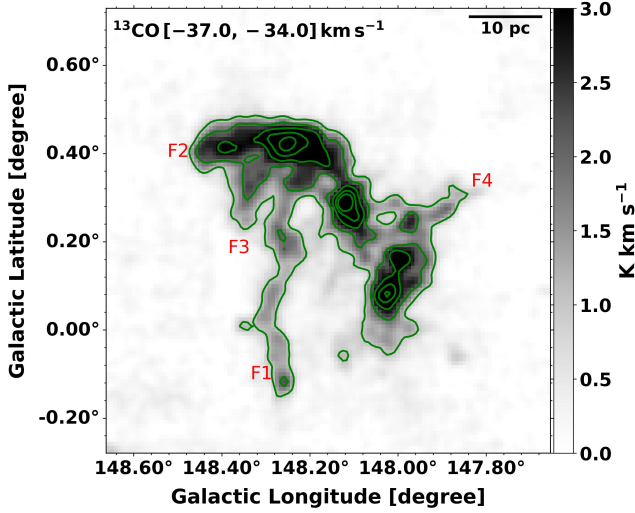


Figure 10. ^{13}CO integrated intensity map in the sub-velocity range, -37.0 to -34.0 km s^{-1} . The filamentary features- F1, F2, and F3 are prominent in this velocity range. Filament-F4 is also visible here.

from the hub, while the head is referred to as the tip of the filaments near the hub.

In filamentary clouds, the observed velocity gradient along the long axis of the filaments is referred to as the longitudinal in-fall motion of the gas. To assess the amplitude of the longitudinal flow along the filaments' long axis, we estimate the velocity gradient of each filament by doing the linear fit to the observed velocity profile along their spines. In some filaments (e.g. F6), noticeable fluctuations in the velocity profiles are seen. Similarly, for filaments F1 and F4, we see a negative velocity gradient towards the tail of the filaments. This could be due to the local gravitational effect of the compact structures and associated star formation activity (e.g. Peretto et al. 2014; Yang et al. 2023). For example, in F1, a noticeable dense compact gas is seen in the tail (see Fig. 11), which might have reversed the flow of direction due to local gravity. Similar situations have also been seen in other filaments as well, for example, see Filament Fi-NW of the SDC 13 hub filamentary system (Peretto et al. 2014).

From the linear fit, the overall velocity gradient along the filament- F1, F2, F3, F4, F5, and F6 are found to be 0.04, 0.06, 0.02, 0.06, 0.06, and 0.03 $\text{km s}^{-1}\text{pc}^{-1}$, respectively. We note that the observed velocities are line-of-sight projected velocities, and thus, small velocity gradients in some filaments could be due to the filament orientation close to the plane-of-sky. Filaments with low inclination angles would make any identification of gas flows along the filaments very difficult. None the less, the observed velocity gradient for most of the filaments is close to the velocity gradient observed in large-scale giant molecular filaments (GMFs), i.e. filaments with lengths > 10 pc. (e.g. Ragan et al. 2014; Wang et al. 2015; Zhang et al. 2019). For example, Ragan et al. (2014) found $0.06 \text{ km s}^{-1}\text{pc}^{-1}$, as an average of the 7 filaments in their sample. Similarly, Wang et al. (2015) find velocity gradient in the range 0.07 – $0.16 \text{ km s}^{-1}\text{pc}^{-1}$ in their sample of GMFs. Similar gradients have also been seen in some large-scale individual filaments (e.g. Hernandez & Tan 2015; Zernickel 2015; Wang et al. 2016). Higher velocity gradients have been observed in filaments at parsec and sub-parsec scales with high-resolution data, particularly in those filaments/elongated structures that are close to the hub or massive clumps (e.g. Liu et al. 2012; Chen et al. 2020; Zhou et al. 2022, 2023). The general finding is that the velocity differences (δV) between the filaments and central clump/hub become

larger as they approach the central clump (i.e. $\delta V \propto \delta R^{-1}$, where δR is the distance to the clump; e.g. see Hacar et al. 2022). This is also observed in G148.24+00.41 as in the proximity of hub (i.e. within the distance of 3 pc), we find that the associated filaments F2 and F6 show higher velocity gradients, $\sim 0.2 \text{ km s}^{-1}\text{pc}^{-1}$, towards their respective heads, which can be seen from Fig. 14. Fig. 14a shows the Position-Velocity (PV) diagram of the central filamentary area covering (see Fig. 8) spines of the filaments F2 and F6 (marked in Fig. 11). The figure also shows the positions of the clumps identified in Section 3.3. Fig. 14b shows the gas velocity variation along the arrows marked in Fig. 14a. The gas profile shows a dip in the PV diagram, like the V-shaped structure found in other filaments, which is considered as a signature of gas inflow along the filaments towards a hub/clump (e.g. Zhou et al. 2022).

To understand the level of turbulence in the filaments, we also calculated the non-thermal velocity dispersion (σ_{nt}) and Mach number ($M = \sigma_{\text{nt}}/c_s$) from the observed velocity dispersion. We calculate the non-thermal velocity dispersion (σ_{nt}) from the total observed velocity dispersion (σ_{obs}) using the relation,

$$\sigma_{\text{nt}} = \sqrt{\sigma_{\text{obs}}^2 - \sigma_{\text{th}}^2}, \quad (8)$$

where $\sigma_{\text{th}} = \sqrt{k_B T_K / \mu_i m_H}$ is the thermal velocity dispersion. T_K is the gas kinetic temperature, k_B is the Boltzmann constant, and μ_i is the mean molecular weight of the observed tracer (e.g. $\mu(^{13}\text{CO}) = 29$ & $\mu(\text{C}^{18}\text{O}) = 30$). The mean σ_{obs} is obtained from the velocity dispersion (moment-II) map within the filament region. Using the average T_{ex} of the filaments as T_{kin} , we calculated the σ_{th} and σ_{nt} of the filaments. Using σ_{nt} and thermal sound speed, $c_s = \sqrt{k_B T_K / \mu m_H}$ with mean molecular weight per free particle, $\mu = 2.37$ (Kauffmann et al. 2008), we can also calculate the total effective velocity dispersion

$$\sigma_{\text{eff}} = \sqrt{\sigma_{\text{nt}}^2 + c_s^2}, \quad (9)$$

The Mach number for the filaments is tabulated in Table 2. The gas in the individual molecular filaments of G148.24+00.41 is found to be supersonic with sonic Mach number ~ 2 – 6^3 . This is in agreement with the results of Wang et al. (2015) and Mattern et al. (2018) toward a sample of large-scale filaments measured with the low-resolution (30 – $46''$) ^{13}CO data using Galactic Ring Survey and SEDIGISM survey data (for details, see Table. 1 of Schuller et al. 2021). However, we want to stress that the derived properties are from the medium-density tracers such as ^{13}CO , but the high-density tracers that would trace very central regions of the filament may give different results. For example, Pineda et al. (2010) comparing high-density and low-density tracers suggested that the sub-sonic turbulence is surrounded by supersonic turbulence in the filaments of the Perseus cloud. Results from high-resolution observations also show that the velocity dispersions of resolved nearby filaments and fibres are close to the sonic or sub-sonic speed (e.g. Hacar et al. 2013; Friesen et al. 2016; Hacar et al. 2017; Saha et al. 2022). All these results tend to suggest that the level of turbulence is scale-dependent,

³ The velocity dispersion may be overestimated if the molecular lines are optically thick (Goldsmith & Langer 1999; Hacar et al. 2016). Along the spine, the optical depth of the ^{13}CO emission for most of the filaments is close to 1. Following the suggestion made by Hacar et al. (2016), this would increase the line width only by 15%, suggesting that even after applying the optical depth correction to the line width, the filaments would remain supersonic.

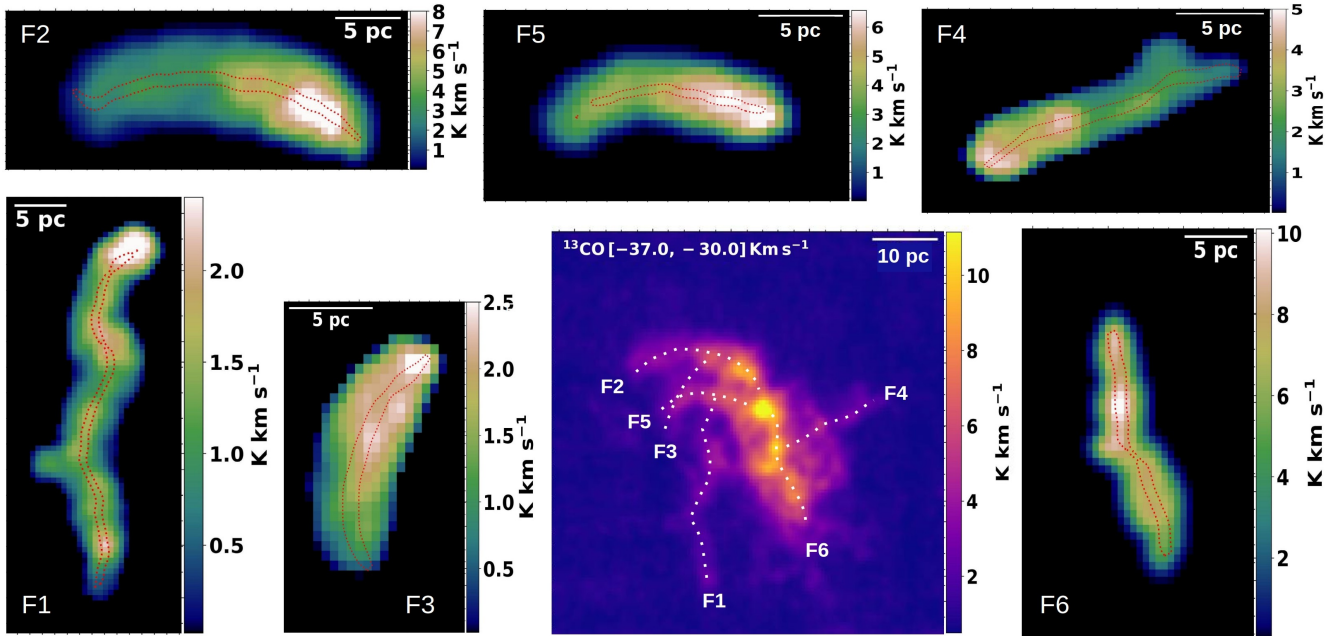


Figure 11. ^{13}CO integrated intensity maps of individual filaments. The red-dotted curve in each filament map shows the filament spine extracted from *Filfinder*.

and subsonic velocity coherent filaments possibly condense out of the more turbulent ambient cloud/filament.

From Fig. 13, we also noticed that the majority of filaments exhibit an increasing velocity dispersion as they approach the hub or ridge. The figure also shows that in the majority of the filaments, the increase in velocity dispersion is proportional to the column density of the gas as we move from the tail to the head of the filaments, which is also evident in the integrated intensity maps shown in Fig. 11. In filaments, strong velocity gradients due to rotation have also been observed, but primarily at smaller scales, such as close to the dense clump or along the minor axis of the filaments. In the present case, the velocity gradients along the long-axis of the filaments over large scale (> 5 pc), as well as the increase in velocity dispersion and column density as they approach the bottom of the potential well of the cloud, suggest for longitudinal flow of gas along the filaments toward the hub/ridge as found in numerical simulations (e.g. Heitsch et al. 2008; Carroll-Nellenback et al. 2014; Vázquez-Semadeni et al. 2019).

3.3 Dense Clumps and Properties

Fig. 3 suggests that the cloud has fragmented into several clumpy structures. These are the clumps of the cloud where star formation could take place. In order to understand the properties and dynamics of these clumps, we utilized C^{18}O data, as it is a better tracer of denser gas and found to be optically thin in G148.24+00.41.

3.3.1 Identification of clumps

For identifying clumps of G148.24+00.41, we implemented the dendrogram (Rosolowsky et al. 2008) method using ASTRODENDRO python package⁴. The dendrogram is a structure-finding algorithm

that identifies hierarchical structures in the input two- or three-dimensional array. The output of the dendrogram depends on three parameters: the *minimum value* that defines the background threshold, the *minimum delta or difference* that defines the separation between two substructures, and the *minimum pixels* that defines the minimum number of pixels or size needed for the structure to be called an independent entity. We ran the dendrogram over the C^{18}O integrated intensity map to find the clumps. We carefully investigate and set the following optimum extraction parameters to detect parsec scale clumpy structures while avoiding faint noisy structures. We set the minimum value to be 3σ above the mean background emission, the minimum delta to be 1σ , and the minimum size to be 12 pixels. Doing so, we identified seven clumps in the cloud, which are marked in Fig. 15a as C1 to C7. The ID, size, and position angle of the clumps are tabulated in Table 3.

3.3.2 Properties of the clumps

We estimated the mass of the clumps using the integrated intensity emission within the clump boundary, the average excitation temperature from the excitation temperature map shown in Fig. 5, and equations 4, 5, and 7 described in Section 3.1.2. The clumps are found to be massive with masses in the range $260\text{--}2100 M_{\odot}$, with the most massive being the central clump, C1, associated with the hub of the cloud. The second most massive clump (C2) is of mass $\sim 1800 M_{\odot}$. The mass of C2 is likely an upper limit, as the clump is possibly tracing the part of the filament that connects C1 and C2. The effective radius (R_{eff}) of the clump is calculated as \sqrt{ab} , where a and b are the semi-major and semi-minor axes of the clump (given in Table 3). The R_{eff} of the clumps are found to be in the range $0.8\text{--}1.9$ pc, with a mean value of ~ 1.4 pc.

Velocity dispersion can reflect the level of turbulence in clumps, and the mean line-width, ΔV of the clump is related to the velocity dispersion (σ_{obs}) as $2.35\sigma_{\text{obs}}$. We get the observed velocity dispersion by fitting a Gaussian profile over the C^{18}O spectrum of the clumps. Fig. 15b shows the average spectral profile of all the

⁴ <http://www.dendrograms.org/>

Table 3. Clump properties. The mass, line-width ($\Delta V = 2.35\sigma_{\text{obs}}$), virial parameter (α), and the ratio of non-thermal velocity dispersion (σ_{nt}) to thermal sound speed (c_s) are calculated using the C^{18}O molecular line data.

Clump	Major axis (pc)	Minor axis (pc)	Position angle (deg)	Mean $\text{N}(\text{H}_2)$ ($\times 10^{21} \text{ cm}^{-2}$)	Mass (M_\odot)	T_{ex} (K)	ΔV (km s^{-1})	α	$\frac{\sigma_{\text{nt}}}{c_s}$
C1	2.2	1.4	219.16	16.1	2100	11.3	1.36	0.2	3.0
C2	2.5	1.5	104.45	9.0	1800	10.5	2.02	0.6	4.5
C3	1.9	1.4	200.56	8.8	1600	11.5	1.67	0.4	3.5
C4	2.0	1.0	220.56	6.1	820	8.8	1.08	0.3	2.6
C5	1.4	0.7	218.06	3.8	260	8.0	0.49	0.1	1.2
C6	1.1	0.5	108.68	6.3	280	10.4	1.18	0.5	2.6
C7	1.6	1.0	142.86	7.2	730	10.0	1.46	0.5	3.3

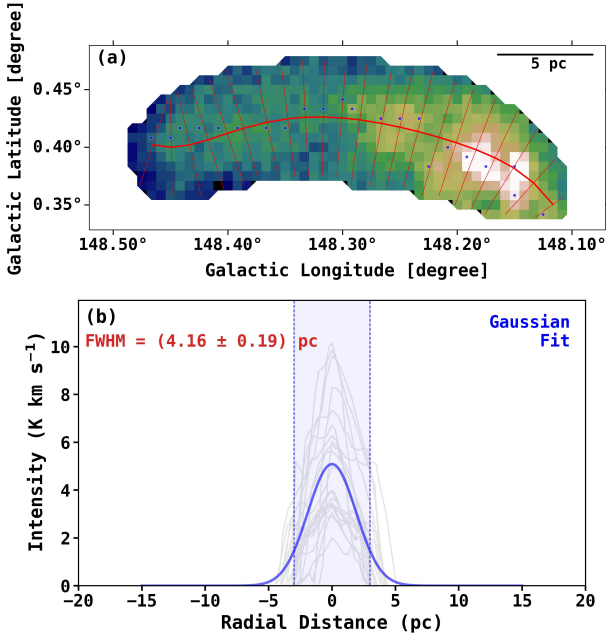


Figure 12. (a) The filament spine of F2 (red solid curve) shown over the ^{13}CO integrated intensity emission, integrated in the velocity range, $[-37.0, -34.0] \text{ km s}^{-1}$. (b) The radial profile of filament F2, built by sampling radial cuts (red solid lines perpendicular to filament spine shown in panel a) at every 2 pixels (roughly 1 beam size $\sim 52''$ or 0.9 pc). The radial distance at a given cut is the projected distance from the peak emission pixel, shown by blue dots in panel a. The grey dots trace the profile of each perpendicular cut, and the blue solid curve shows the Gaussian fit over these filament profiles. The light-blue shaded region shows the range of radial distance taken for the Gaussian fit.

clumps. The velocity dispersion of the clumps is in the range of 0.21 to 0.86 km s^{-1} , with a mean value of 0.56 km s^{-1} . As determined for the whole cloud, one can also infer whether the clumps are bound or not by calculating the virial parameter, $\alpha = \frac{M_{\text{vir}}}{M_c}$, where M_{vir} and M_c are the virial mass and gas mass of the clumps, respectively. We calculated M_{vir} using density index, $\beta = 2$, by assuming a spherical density profile for the clumps. The R_{eff} , mean T_{ex} , ΔV , M_c , and α values of the clumps are tabulated in Table 3. The α value of all the clumps is found to be less than 2, suggesting that they are gravitationally bound and, thus, would form or are in the process of forming stars. This will also remain true even if we take $\beta = 1.5$.

To determine the contribution of non-thermal (turbulent) support against gravity in the clumps, we calculate the non-thermal veloc-

ity dispersion and total effective velocity dispersion from the total observed velocity dispersion, using the same procedures outlined in Section 3.2.5. Fig. 15c shows the σ_{nt} , c_s , and σ_{eff} values of the clumps based on C^{18}O data. From the figure, it can be seen that for all the clumps, the non-thermal velocity dispersion or the turbulence contribution is more dominant than the thermal component. Using the ratio σ_{nt}/c_s , we calculate the Mach number, which is given in Table 3. The Mach number lies in the range of 1.2 to 4.5, with a mean of around 3. Thus, the clumps have supersonic non-thermal motions. The non-thermal motions could be either due to small-scale gas motions within the clump or protostellar feedback due to local star formation activity or a combination of both the processes. For example, Rawat et al. (2023) discussed that the hub is also associated with a massive YSO (Young Stellar Object) with an outflow, thus, its radiation and feedback might have also impacted the dynamics of the surrounding gas.

4 DISCUSSION

4.1 Stability of the Filaments

The stability of the filament can be evaluated by comparing its observed line mass, M_{line} , with the critical line mass, M_{crit} . Assuming filaments are in cylindrical hydrostatic equilibrium, M_{crit} is expressed as (Fiege & Pudritz 2000):

$$M_{\text{crit}} = \frac{2\sigma_{\text{eff}}^2}{G} \sim 464 \sigma_{\text{eff}}^2 (M_\odot \text{ pc}^{-1}), \quad (10)$$

where σ_{eff} is the effective velocity dispersion in km s^{-1} and G is the gravitational constant. The filament is unstable to axisymmetric perturbation if its line mass exceeds its critical line mass (Inutsuka & Miyama 1992). In the case of isothermal filament, $\sigma_{\text{eff}} = c_s$, where c_s is the sound speed of the medium (e.g. Ostriker 1964). In this scenario, the critical line mass only depends on the gas temperature. The average temperature (T_{ex}) of the filaments estimated within their widths lies in the range 8–10 K, which corresponds to $M_{\text{crit}} \sim 13\text{--}17 M_\odot \text{ pc}^{-1}$. The line masses for the filaments that we estimated with our data are significantly above the critical thermal line mass. This suggests that either the filaments are collapsing radially or they are supported by additional mechanisms such as non-thermal turbulent motions. These turbulent motions can be generated either due to already formed stars within the filaments or by the radial accretion/infall of the surrounding gas onto the filaments (Hennebelle & André 2013; Clarke et al. 2016). The presence of non-thermal motions would increase the effective sound speed, thereby would

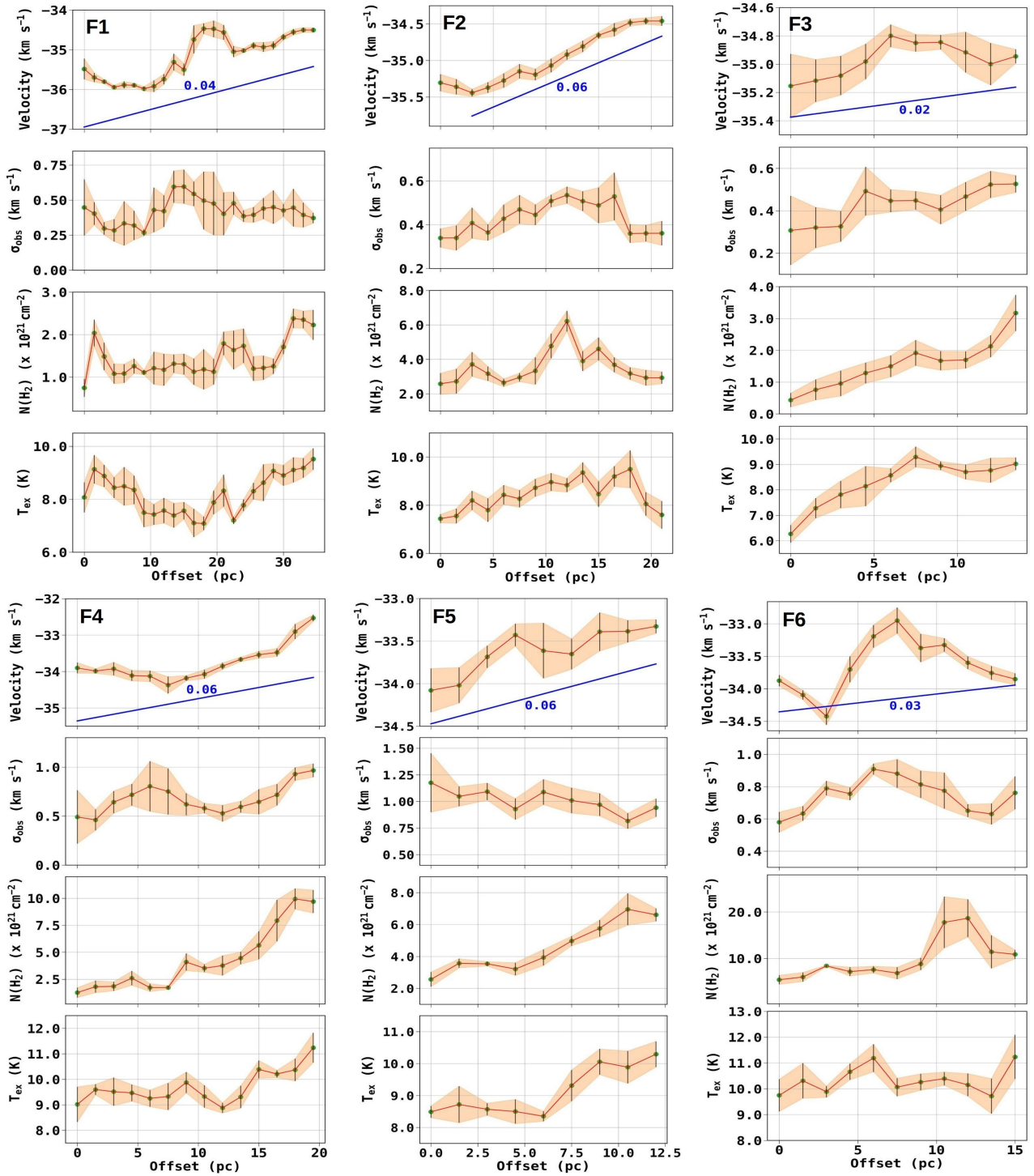


Figure 13. The average velocity, velocity dispersion, column density, and excitation temperature as a function of distance from the filament tail to the head, determined using ^{13}CO . The offset 0 pc is at the filament tail. The error bars show the statistical standard deviation at each point. The blue solid line in the top panel of each filament plot shows the linear fit to the data points, whose slope (marked in the plot) gives the velocity gradient along the filament.

increase the effective velocity dispersion ($\sigma_{\text{eff}} = \sqrt{c_s^2 + \sigma_{\text{nt}}^2}$) of the filament, and thus, the critical line mass. At present, the observed velocity dispersion along the filament is higher than that one would expect for a cloud with a temperature in the range 10–15 K. Therefore, to understand the present dynamical status of the filaments, we compute the M_{crit} for the filaments assuming that they are supported

by thermal as well as non-thermal motions. Using the mean effective velocity dispersion of the filaments (0.44, 0.45, 0.44, 0.68, 1.03, and 0.78 km s^{-1}), we calculated the M_{crit} values as 90, 94, 90, 215, 496, and 283 $M_{\odot} \text{ pc}^{-1}$ for F1, F2, F3, F4, F5, and F6, respectively, with a mean value around $\sim 211 M_{\odot} \text{ pc}^{-1}$.

Arzoumanian et al. (2019) based on *Herschel* analysis and considering thermal line mass as the critical mass, categorised the filaments

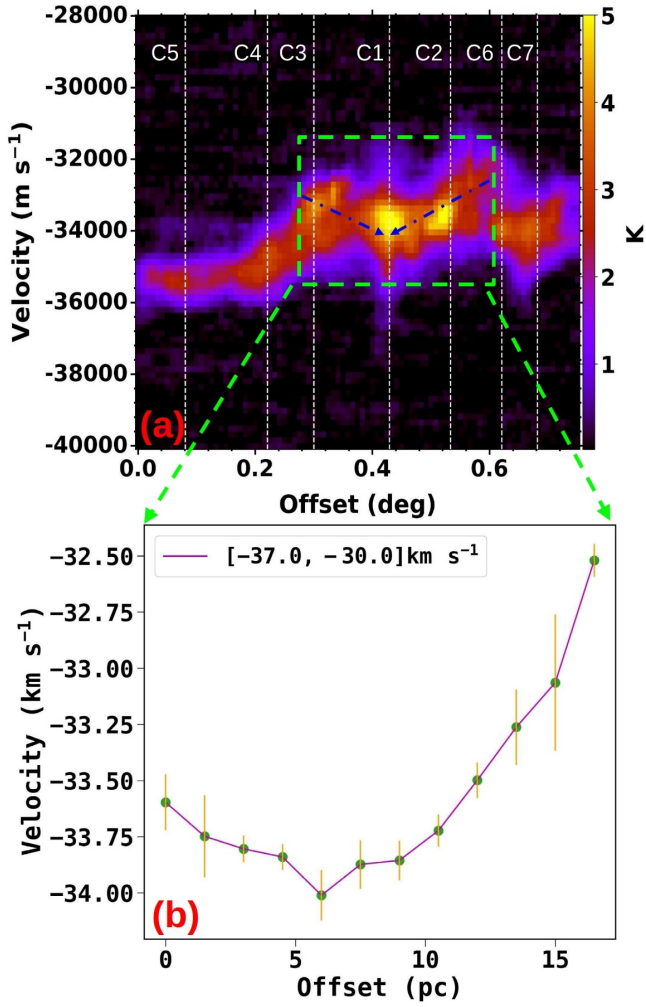


Figure 14. (a) The position-velocity (PV) diagram of the full ridge based on ^{13}CO , which is shown in Fig. 9. The green-dashed box shows the region that is used to see the gas flow structure along the blue dashed-dotted arrows, toward the central hub/clump. The vertical dashed lines show the location of identified clumps, marked with their names. (b) The variation of average velocity with distance along the arrows (shown in panel a), which shows the velocity gradient towards the central hub/clump.

of the nearby clouds as supercritical filaments ($M_{\text{line}} \geq 2 M_{\text{crit}}$), transcritical filaments ($0.5 M_{\text{crit}} \leq M_{\text{line}} < 2 M_{\text{crit}}$), and subcritical filaments ($M_{\text{line}} \leq 0.5 M_{\text{crit}}$). They suggested that thermally subcritical filaments are gravitationally unbound entities, while transcritical and supercritical filaments are the preferable sites for gravitational collapse and core formation. Based on the thermal line mass, all of our filaments are super-critical, thus, might have undergone collapse and sub-sequence fragmentation to form cores. This fact is evident from the distribution of protostars on the filaments, shown in Fig. 16. The figure shows that most of the protostars have been formed in the ridge/F6 of the G148.24+00.41 cloud, and a few protostars seem to be formed at the head of the filaments F1, F2, and F5. Taking the contribution of non-thermal motion, we find that the line mass of F1, F2, F3, and F6 is larger than their M_{crit} values, suggesting that they are still gravitationally unstable, whereas for F4 and F5, the M_{line} is smaller than the M_{crit} value, suggesting that they are possibly stable against collapse. However, we note that the line masses are estimated with canonical values of ^{12}C to ^{13}C isotope ratio and can be higher

by a factor of 1.3, if isotopic ratio at the galactocentric distance of the cloud is considered (e.g. Pineda et al. 2013).

In the above discussion, we have investigated the dynamical status of the filaments, however, we note that in the dynamical scenario of cloud formation and evolution, filaments are very likely to deviate from true equilibrium structures. Because in the dynamical scenario of cloud collapse, filaments are described as dynamical structures that continuously accrete from the ambient gas while feeding dense cores within them. Moreover, it has also been found that due to the gravitational focusing effect, finite filaments are more prone to collapse at the ends of their long axis (Burkert & Hartmann 2004; Pon et al. 2011), even when such filaments are subcritical. Thus, though the average properties of some of the filaments are sub-critical, they have a higher concentration of column density at their heads due to longitudinal flow along their axis, where filaments can transit from sub-critical to super-critical.

4.2 Mass flow Along the Filament Axis

Assuming that the observed velocity gradient in filaments is due to gas accretion flow, we estimate the mass accretion rate, \dot{M}_{\parallel} along the filaments using a simple cylindrical model and relation given in Kirk et al. (2013),

$$\dot{M}_{\parallel} = V_{\parallel} \times \rho(\pi r^2) = V_{\parallel} \left(\frac{M}{L} \right), \quad (11)$$

where V_{\parallel} is the velocity along the filament, which is multiplied by the density, $\rho = \left(\frac{M}{\pi r^2 L} \right)$, and the perpendicular area (πr^2) of the flow. The r , M , and L are the radius, mass content, and length of the cylinder, respectively. By taking the plane of sky projection with an inclination angle, α , the observed parameters of the cylinder are: $L_{\text{obs}} = L \cos(\alpha)$, $V_{\parallel, \text{obs}} = V_{\parallel} \sin(\alpha)$, and $V_{\perp, \text{obs}} = \Delta V_{\parallel, \text{obs}} L_{\text{obs}}$. After simplification, the \dot{M}_{\parallel} expression reduces to

$$\dot{M}_{\parallel} = \frac{\Delta V_{\parallel, \text{obs}} M}{\tan(\alpha)}, \quad (12)$$

where, $\Delta V_{\parallel, \text{obs}}$ is the observed velocity gradient along the filament. Taking the obtained mass and velocity gradient of the filaments (see Table 2), and $\alpha = 45^\circ$ (Kirk et al. 2013), the estimated mass accretion rate for filament F1, F2, F3, F4, F5, and F6 is around $\sim 140, 264, 26, 150, 204$, and $207 M_{\odot} \text{ Myr}^{-1}$, respectively. Among which, the filaments F2, F5, and F6 are directly tied to the hub (see Fig. 11), whose combined accretion rate is around $\sim 675 M_{\odot} \text{ Myr}^{-1}$. We note that the combined mass-accretion rate to the hub is an upper limit as the F6 filament will not transfer its mass entirely to the central hub due to the presence of an additional clump competing with it in the filament. However, we have not accounted for the contribution of small-scale filaments attached to the hub, as seen in the *Herschel* dust continuum image (Fig 14 of Rawat et al. 2023), which would conversely add to the combined accretion rate.

Taking the above-measured accretion rate as a face value, we find that it is either comparable or higher than some of the well-known cluster-forming hubs found in the literature, such as Mon R2 ($400\text{--}700 M_{\odot} \text{ Myr}^{-1}$, Treviño-Morales et al. 2019), Serpens ($100\text{--}300 M_{\odot} \text{ Myr}^{-1}$, Kirk et al. 2013), Orion ($385 M_{\odot} \text{ Myr}^{-1}$, Rodríguez-Franco et al. 1992; Hacar et al. 2017), the DR 21 ridge ($1000 M_{\odot} \text{ Myr}^{-1}$, Schneider et al. 2010), G326.27-0.49 ($970 M_{\odot} \text{ Myr}^{-1}$, Mookerjee et al. 2023), and G310.142+0.758 ($700 M_{\odot} \text{ Myr}^{-1}$, Yang et al. 2023). This comparison, however, should be treated with caution because all these measurements have been done

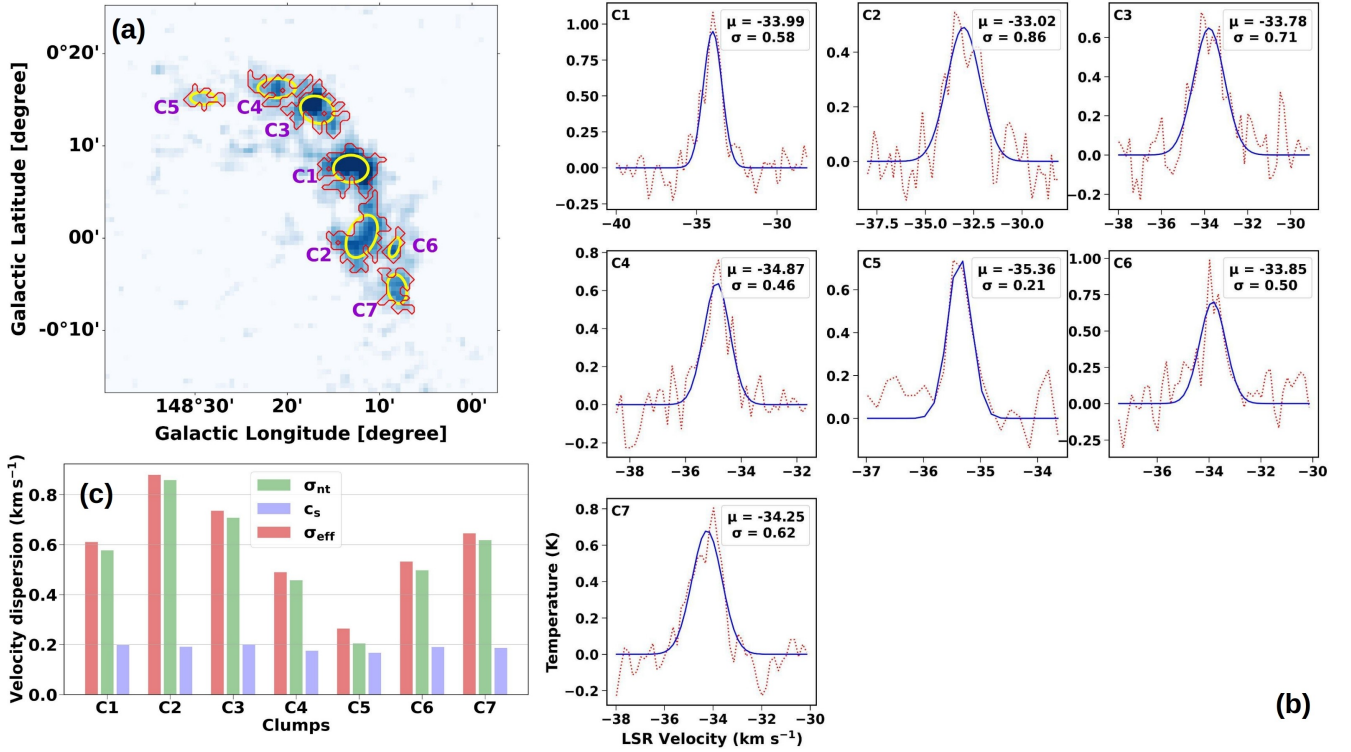


Figure 15. (a) The location of the clumps identified using ASTRODENDRO over $C^{18}O$ intensity map. The red contours show the leaf structures identified using dendrograms, and the ellipses show the clump within them. (b) The average $C^{18}O$ spectral profile of the clumps over which the solid blue curve denotes the best-fit Gaussian profile, and their respective mean and standard deviation are given in each panel. (c) The histogram plot of non-thermal (σ_{nt}), thermal sound speed (c_s), and the total effective (σ_{eff}) velocity dispersion of the clumps.

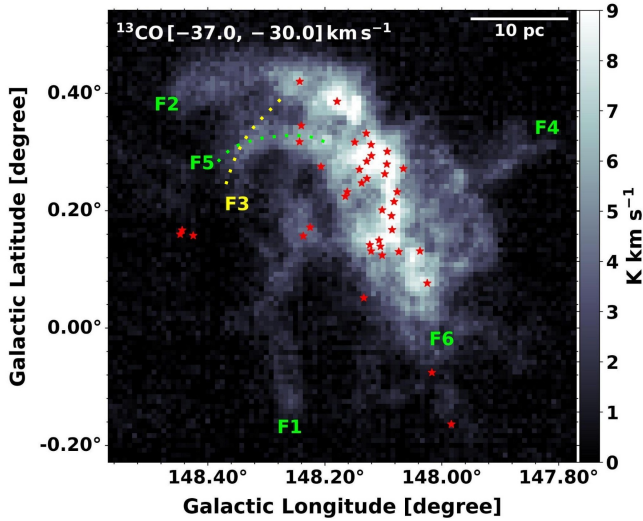


Figure 16. The distribution of protostars from *Herschel* 70 micron point source catalogue (*Herschel Point Source Catalogue Working Group et al. 2020*) on the ^{13}CO integrated intensity map.

with different tracers having different resolutions that cover different scales around the hubs. Measuring the accretion rate for massive clouds that have hub filamentary systems, such as those mentioned above, in a uniform way, would give more valuable insight into the accretion rate and the mass assembly time scales of such systems.

4.3 Overview of Cluster Formation Processes in G148.24+00.41

[Rawat et al. \(2023\)](#) studied the cloud's profile, structure, and fractalness, as well as the spatial, temporal, and luminosity distribution of the protostars with respect to the cloud's central potential, and suggested that the cloud is likely in a state of hierarchical collapse.

[Vázquez-Semadeni et al. \(2019\)](#) suggested that due to non-homologous collapse in molecular clouds, a classical signature of spherical collapse is not expected over a larger scale. However, at the clump scale, a global velocity offset between peripheral ^{12}CO and internal ^{13}CO , as found by [Barnes et al. \(2018\)](#), is a signature of collapse. According to [Barnes et al. \(2019\)](#), if the average ^{12}CO profile is red-shifted with respect to the average ^{13}CO profile, the motion of the enveloping ^{12}CO gas is inwards, while if it is blue-shifted, then the motion is outwards. Fig. 17b shows the line profiles of the CO -molecules within the 3 pc area (marked by the red rectangle in Fig. 17a) around the hub. The figure shows that the ^{12}CO profile is redshifted with respect to ^{13}CO profile, inferring the net inward motion of ^{12}CO envelope ([Barnes et al. 2018](#)). However, to get the conclusive signature of infall motion at the clump scale, we need high-density tracer data ([Yuan et al. 2018](#); [Liu et al. 2020](#); [Yang et al. 2023](#)).

In G148.24+00.41, there are six filaments with converging flows heading towards the hub of the cloud. For the filaments having aspect ratio, $A_0 = Z_0/R_0 \gtrsim 2$, one can calculate the longitudinal collapse timescale using a single equation, $t_{COL} \sim (0.49 + 0.26A_0)(G\rho_0)^{-1/2}$ ([Clarke & Whitworth 2015](#)), where Z_0 , R_0 , and $\rho_0 = M_{line}/\pi R_0^2$ is the half-length, radius, and density of the filament, respectively. In our case, the aspect ratio of all the filaments is greater than 2. Using the aforementioned formalism, we find that the longitudinal collapse

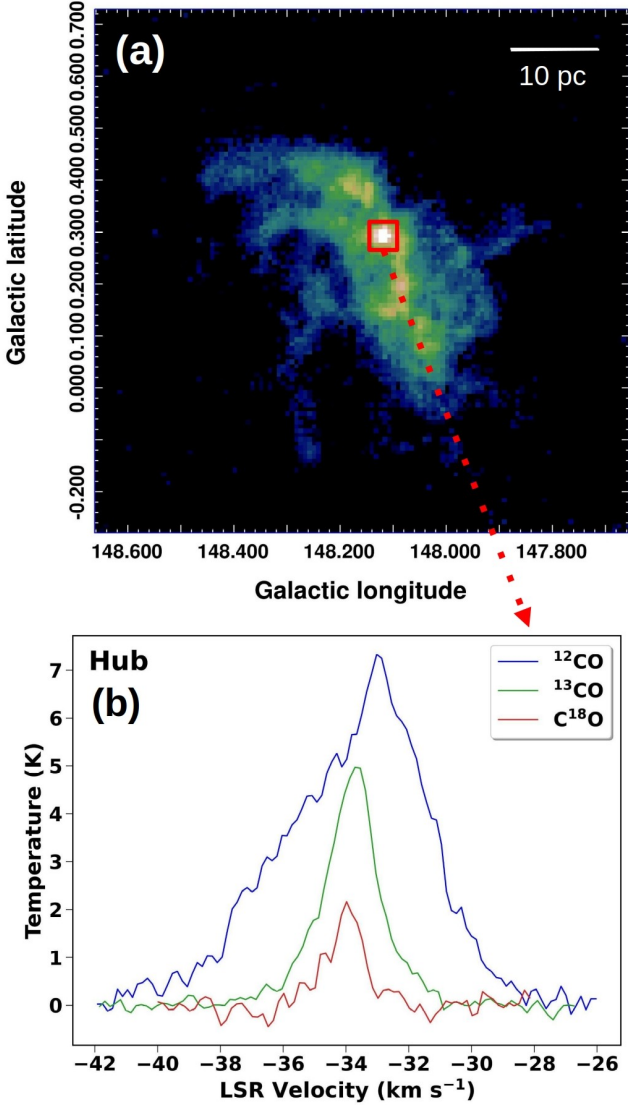


Figure 17. (a) The ^{13}CO integrated intensity map showing the location of the hub by a red box, having size $\sim 3.5 \times 3.0$ pc. (b) The average ^{12}CO , ^{13}CO , and C^{18}O spectral profile of the hub region (shown in panel a).

timescale of these filaments is in the range of 5–15 Myr, while the free-fall time of the central clump ($t_{ff} = \sqrt{3\pi/32G\rho_c}$, where ρ_c is the density of the clump) is found to be ~ 1 Myr. Since in dynamical hierarchical collapse, each scale accretes from a larger scale, implying that the filaments may continue to fuel the clump for a longer time, provided that they remain bound. Taking the upper limit of combined inflow rate to the C1-clump as $\sim 675 \text{ M}_\odot \text{ Myr}^{-1}$, we estimate that to assemble the current mass of the clump, i.e. $\sim 2100 \text{ M}_\odot$, a minimum time of ~ 3 Myr would be needed, while the age of the cloud based on formed young stellar objects is around 0.5–1 Myr (for details, see Rawat et al. 2023). This implies that while the mass assembly is ongoing towards the clump, the star formation in the cloud might have initiated around 0.5–1 Myr ago. However, we acknowledge that our estimated mass assembly time scale to the C1-clump can be an upper limit due to the following reasons: i) the accretion rate was higher during the early phase of cloud evolution, ii) overestimation of the clump mass due to low-resolution data, iii) missing the contribution of other small-scale filaments such as

those seen in *Herschel* images, or a combination of all. Future high-resolution observations focusing on the clump area would shed more light on the latter two hypotheses. None the less, the derived accretion rate is close to those found in some of the well-known cluster-forming hub-filamentary systems (discussed in Section 4.2) and also to the prediction of massive cluster-forming simulations (e.g. Vázquez-Semadeni et al. 2009; Howard et al. 2018). For example, Vázquez-Semadeni et al. (2009) using numerical simulations, suggest that the formation of massive stars or clusters is associated with large-scale collapse involving thousands of solar masses and accretion rates of $\sim 10^{-3} \text{ M}_\odot \text{ yr}^{-1}$.

The G148.24+00.41 cloud has fragmented into seven massive clumps in the range of 260–2100 M_\odot , and the majority of them have the potential to form an independent group of stars or cluster (e.g. to form a massive star and associated cluster, a minimum mass $\geq 300 \text{ M}_\odot$ is needed; see Appendix A in Sanhueza et al. 2019). However, our search for the presence of embedded sources within the clumps using mid-infrared data (i.e. using $3.6 \mu\text{m}$ *Spitzer* images) resulted that the massive clumps are associated with stellar sources, and the hub (i.e. the clump C1) hosts the most compact and richer stellar group. Rawat et al. (2023) also found that the most luminous ($\sim 1900 L_\odot$) protostar of the complex is located within the hub. Thus, we hypothesize that in the G148.24+00.41 cloud, the cluster formation in the hub is facilitated by filamentary accretion flows from large-scale cloud to small-scale clumps/hub, which can either be gravity-driven (GHC; Gómez & Vázquez-Semadeni 2014; Vázquez-Semadeni et al. 2019) or turbulence-driven (I2; Padoan et al. 2020). The cluster in the hub has the potential to grow into a richer cluster by gradually accumulating additional cold gas. Rawat et al. (2023), based on the spatial and temporal distribution and fractal subclustering of the stellar sources in G148.24+00.41, suggest that GHC may be the dominant mechanism responsible for the formation of the stellar cluster in this cloud. Based on the low-resolution CO data, used in this work, it is difficult to distinguish between the aforementioned two models. Future shock tracer observational data would be helpful in this regard, as the I2 model suggests the formation of filaments due to shocks, while in GHC, the filaments form due to large-scale gravity flow (Yang et al. 2023). Figure 18 illustrates the potential structure and overall gas kinematics of the cloud, forming clusters at the nodes of the filamentary flows, with the richest cluster being located at the bottom of the cloud’s potential.

5 SUMMARY AND CONCLUSION

In the present work, we studied the gas properties and kinematics of the cloud. Based on CO analysis, we confirm that the cloud is massive ($\sim 10^5 \text{ M}_\odot$), bound, and hosts a massive clump of mass $\sim 2100 \text{ M}_\odot$ nearly at its geometric centre. Based on the low-resolution ^{13}CO data, in the present work, we identified six likely velocity coherent, large-scale (length > 10 pc and aspect ratio > 4) filamentary structures in the cloud. Out of which, three filaments (namely F2, F5, and F6) are directly tied to the clump located in the hub. We could not identify and characterize three relatively small-scale filaments that are attached to the hub as seen in the *Herschel* images, thus, their role and properties are not investigated in this work. Among the studied filaments, we find that most of them are massive, with high mass per unit length, M_{line} . We estimated that each filament has the potential to fuel the cold gaseous matter at a rate ranging from 26 to $264 \text{ M}_\odot \text{ Myr}^{-1}$ to the centre of the cloud.

The filaments have undergone fragmentation as several protostars (age $\leq 5 \times 10^5$ yr) that are identified using $70 \mu\text{m}$ and $160 \mu\text{m}$

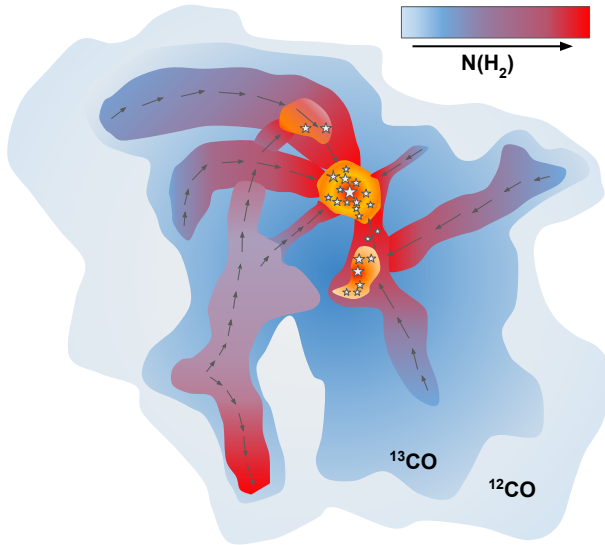


Figure 18. Cartoon illustrating the observed structures in G148.24+00.41. The black arrows represent the directions of the overall gas flow. The background colour displays the local density of ^{12}CO and ^{13}CO .

images by Rawat et al. (2023) are found to be associated with the filaments. Particularly, the filament F6 seems to be associated with a chain of protostars along its spine. The filament F6 has a high line mass, thus possibly actively forming protostars. In the case of the other filaments, the protostars are located close to their respective head, where strong density enhancement is seen in their respective integrated intensity map. These density enhancements could be due to the filamentary accretion flows along their long axis towards the bottom of the potential well, i.e. towards the hub location. In fact, the velocity profile of the filaments suggests that each filament is possibly undergoing longitudinal collapse, as the majority of them tend to show a velocity gradient in the range $0.03\text{--}0.06\text{ km s}^{-1}\text{ pc}^{-1}$. These gradients are derived over the entire length of the filaments, i.e. for the length scale of $10\text{--}15\text{ pc}$ and found to be comparable to the gradients of the large-scale filaments. We find that the increase in velocity along the filaments is also correlated with the increase in column density and velocity dispersion. We have also found higher velocity gradients near the hub location (see Fig. 14b), implying the acceleration of gas motion towards the hub. We note that, though the kinematic features are suggestive of large-scale flows toward the hub, but due to the presence of other clumps in the ridge, the kinematics of the filaments are found to be complicated. Future high-resolution observations will be essential to better understand the kinematics and dynamics of the gas in the filaments and the hub, and unveil the multi-scale process of massive cluster formation.

The cloud has fragmented into seven massive clumps having mass in the range $260\text{--}2100\text{ M}_{\odot}$. We found that the clump located at the hub of the cloud is the most massive one, associated with a massive YSO and a stellar cluster. All these evidence suggests that within the cloud, the hub is the dominant place where a prominent cluster is in the process of emerging. Overall, our results are consistent with the flow-driven gas assembly, leading to the formation of the dense clump in the hub and the subsequent emergence of a stellar cluster.

ACKNOWLEDGEMENT

We thank the anonymous referee for the comments and suggestions that helped to improve the paper. The research work at the Physical

Research Laboratory is funded by the Department of Space, Government of India. This research made use of the data from the Milky Way Imaging Scroll Painting (MWISP) project, which is a northern galactic plane CO survey with the PMO-13.7m telescope. We are grateful to all the members of the MWISP working group, particularly the staff members at the PMO-13.7m telescope, for their long-term support. MWISP was sponsored by the National Key R&D Program of China with grant 2017YFA0402701 and CAS Key Research Program of Frontier Sciences with grant QYZDJ-SSW-SLH047. D.K.O. acknowledges the support of the Department of Atomic Energy, Government of India, under project identification No. RTI 4002. We thank Eric Koch and Catherine Zucker, for the discussion on using the *FilFinder* and *RadFil* packages, respectively, to extract the filamentary features and their profiles.

DATA AVAILABILITY

We used the CO molecular data from PMO, which can be shared by the PMO database on reasonable request. We have also used *Herschel* 250 μm image and 70 micron point source catalogue. The *Herschel* images are publicly available from Herschel Science Archive (<http://archi-ves.esac.esa.int/hsa/whsa>) and the *Herschel* point source catalogue is available on Vizier.

REFERENCES

- Adamo A., et al., 2020, *Space Sci. Rev.*, **216**, 69
- André P., et al., 2010, *A&A*, **518**, L102
- André P., Di Francesco J., Ward-Thompson D., Inutsuka S. I., Pudritz R. E., Pineda J. E., 2014, in Beuther H., Klessen R. S., Dullemond C. P., Henning T., eds, *Protostars and Planets VI*. p. 27 ([arXiv:1312.6232](https://arxiv.org/abs/1312.6232)), doi:10.2458/azu_uapress_9780816531240-ch002
- André P., 2017, *Comptes Rendus Geoscience*, **349**, 187
- Arzoumanian D., et al., 2019, *A&A*, **621**, A42
- Banerjee S., Kroupa P., 2015, *MNRAS*, **447**, 728
- Barnes P. J., Hernandez A. K., Muller E., Pitts R. L., 2018, *ApJ*, **866**, 19
- Barnes A. T., et al., 2019, *MNRAS*, **486**, 283
- Beltrán M. T., Rivilla V. M., Kumar M. S. N., Cesaroni R., Galli D., 2022, *A&A*, **660**, L4
- Bolatto A. D., Wolfire M., Leroy A. K., 2013, *ARA&A*, **51**, 207
- Bourke T. L., et al., 1997, *ApJ*, **476**, 781
- Burkert A., Hartmann L., 2004, *ApJ*, **616**, 288
- Cao Y., Qiu K., Zhang Q., Li G.-X., 2022, *ApJ*, **927**, 106
- Carroll-Nellenback J. J., Frank A., Heitsch F., 2014, *ApJ*, **790**, 37
- Castets A., Langer W. D., 1995, *A&A*, **294**, 835
- Chen M. C.-Y., et al., 2020, *ApJ*, **891**, 84
- Clarke S. D., Whitworth A. P., 2015, *MNRAS*, **449**, 1819
- Clarke S. D., Whitworth A. P., Hubber D. A., 2016, *MNRAS*, **458**, 319
- Cox N. L. J., et al., 2016, *A&A*, **590**, A110
- Dame T. M., Hartmann D., Thaddeus P., 2001, *ApJ*, **547**, 792
- Dewangan L. K., Ojha D. K., Sharma S., Palacio S. d., Bhadani N. K., Das A., 2020, *ApJ*, **903**, 13
- Federrath C., 2016, *MNRAS*, **457**, 375
- Fiege J. D., Pudritz R. E., 2000, *MNRAS*, **311**, 85
- Frerking M. A., Langer W. D., Wilson R. W., 1982, *ApJ*, **262**, 590
- Friesen R. K., Medeiros L., Schnee S., Bourke T. L., di Francesco J., Gutermuth R., Myers P. C., 2013, *MNRAS*, **436**, 1513
- Friesen R. K., Bourke T. L., Di Francesco J., Gutermuth R., Myers P. C., 2016, *ApJ*, **833**, 204
- Garden R. P., Hayashi M., Gatley I., Hasegawa T., Kaifu N., 1991, *ApJ*, **374**, 540
- Goldsmith P. F., 2001, *ApJ*, **557**, 736
- Goldsmith P. F., Langer W. D., 1999, *ApJ*, **517**, 209

- Goldsmith P. F., Heyer M., Narayanan G., Snell R., Li D., Brunt C., 2008, *ApJ*, **680**, 428
- Gómez G. C., Vázquez-Semadeni E., 2014, *ApJ*, **791**, 124
- Gómez G. C., Vázquez-Semadeni E., Zamora-Avilés M., 2018, *MNRAS*, **480**, 2939
- Guilloteau S., Lucas R., 2000, in Mangum J. G., Radford S. J. E., eds, *Astronomical Society of the Pacific Conference Series Vol. 217, Imaging at Radio through Submillimeter Wavelengths*. p. 299
- Guo W., et al., 2022, *ApJ*, **938**, 44
- Hacar A., Tafalla M., Kauffmann J., Kovács A., 2013, *A&A*, **554**, A55
- Hacar A., Alves J., Burkert A., Goldsmith P., 2016, *A&A*, **591**, A104
- Hacar A., Alves J., Tafalla M., Goicoechea J. R., 2017, *A&A*, **602**, L2
- Hacar A., Tafalla M., Forbrich J., Alves J., Meingast S., Grossschedl J., Teixeira P. S., 2018, *A&A*, **610**, A77
- Hacar A., Clark S., Heitsch F., Kainulainen J., Panopoulou G., Seifried D., Smith R., 2022, *arXiv e-prints*, p. arXiv:2203.09562
- Heitsch F., Hartmann L. W., Slyz A. D., Devriendt J. E. G., Burkert A., 2008, *ApJ*, **674**, 316
- Hennebelle P., André P., 2013, *A&A*, **560**, A68
- Hennemann M., et al., 2012, *A&A*, **543**, L3
- Hernandez A. K., Tan J. C., 2015, *ApJ*, **809**, 154
- Hernandez A. K., Tan J. C., Caselli P., Butler M. J., Jiménez-Serra I., Fontani F., Barnes P., 2011, *ApJ*, **738**, 11
- Herschel Point Source Catalogue Working Group et al., 2020, *VizieR Online Data Catalog*, p. VIII/106
- Heyer M., Dame T. M., 2015, *ARA&A*, **53**, 583
- Heyer M., Krawczyk C., Duval J., Jackson J. M., 2009, *ApJ*, **699**, 1092
- Howard C. S., Pudritz R. E., Harris W. E., 2018, *Nature Astronomy*, **2**, 725
- Hu B., et al., 2021, *ApJ*, **908**, 70
- Inutsuka S.-I., Miyama S. M., 1992, *ApJ*, **388**, 392
- Kauffmann J., Bertoldi F., Bourke T. L., Evans N. J. I., Lee C. W., 2008, *A&A*, **487**, 993
- Kirk H., Myers P. C., Bourke T. L., Gutermuth R. A., Hedden A., Wilson G. W., 2013, *ApJ*, **766**, 115
- Koch E. W., Rosolowsky E. W., 2015, *MNRAS*, **452**, 3435
- Könyves V., et al., 2015, *A&A*, **584**, A91
- Krause M. G. H., et al., 2020, *Space Sci. Rev.*, **216**, 64
- Krumholz M. R., McKee C. F., 2020, *MNRAS*, **494**, 624
- Krumholz M. R., McKee C. F., Bland-Hawthorn J., 2019, *ARA&A*, **57**, 227
- Kumar M. S. N., Palmeirim P., Arzoumanian D., Inutsuka S. I., 2020, *A&A*, **642**, A87
- Kumar M. S. N., Arzoumanian D., Men'shchikov A., Palmeirim P., Matsumura M., Inutsuka S., 2022, *A&A*, **658**, A114
- Lada C. J., Lada E. A., 2003, *ARA&A*, **41**, 57
- Lada C. J., Lombardi M., Alves J. F., 2010, *ApJ*, **724**, 687
- Lewis J. A., Lada C. J., Dame T. M., 2022, *ApJ*, **931**, 9
- Li H., et al., 2015, *The Astrophysical Journal Supplement Series*, **219**, 20
- Li S., et al., 2022, *ApJ*, **926**, 165
- Liszt H. S., 2017, *ApJ*, **835**, 138
- Liu H. B., Jiménez-Serra I., Ho P. T. P., Chen H.-R., Zhang Q., Li Z.-Y., 2012, *ApJ*, **756**, 10
- Liu T., et al., 2020, *MNRAS*, **496**, 2790
- Liu X.-L., Xu J.-L., Wang J.-J., Yu N.-P., Zhang C.-P., Li N., Zhang G.-Y., 2021, *A&A*, **646**, A137
- Liu H.-L., et al., 2023, *MNRAS*, **522**, 3719
- Longmore S. N., et al., 2014, in Beuther H., Klessen R. S., Dullemond C. P., Henning T., eds, *Protostars and Planets VI*. pp 291–314 (arXiv:1401.4175), doi:10.2458/azu_uapress_9780816531240-ch013
- Mattern M., et al., 2018, *A&A*, **619**, A166
- Miville-Deschênes M.-A., Murray N., Lee E. J., 2017, *ApJ*, **834**, 57
- Molinari S., et al., 2010, *A&A*, **518**, L100
- Mookerjee B., Veena V. S., Güsten R., Wyrowski F., Lasrado A., 2023, *MNRAS*, **520**, 2517
- Motte F., Bontemps S., Louvet F., 2018, *ARA&A*, **56**, 41
- Myers P. C., 2009, *ApJ*, **700**, 1609
- Nakanishi H., Sofue Y., 2006, *PASJ*, **58**, 847
- Naranjo-Romero R., Zapata L. A., Vázquez-Semadeni E., Takahashi S., Palau A., Schilke P., 2012, *ApJ*, **757**, 58
- Nishimura A., et al., 2015, *ApJS*, **216**, 18
- Ostriker J., 1964, *ApJ*, **140**, 1056
- Padoan P., Pan L., Juvela M., Haugbølle T., Nordlund Å., 2020, *ApJ*, **900**, 82
- Panopoulou G. V., Psaradaki I., Skolidis R., Tassis K., Andrews J. J., 2017, *MNRAS*, **466**, 2529
- Panopoulou G. V., Clark S. E., Hacar A., Heitsch F., Kainulainen J., Ntormousi E., Seifried D., Smith R. J., 2022, *A&A*, **657**, L13
- Patra S., II N. J. E., Kim K.-T., Heyer M., Kauffmann J., Jose J., Samal M. R., Das S. R., 2022, *The Astronomical Journal*, **164**, 129
- Peretto N., et al., 2014, *A&A*, **561**, A83
- Pineda J. E., Caselli P., Goodman A. A., 2008, *ApJ*, **679**, 481
- Pineda J. L., Goldsmith P. F., Chapman N., Snell R. L., Li D., Cambrésy L., Brunt C., 2010, *ApJ*, **721**, 686
- Pineda J. L., Langer W. D., Velusamy T., Goldsmith P. F., 2013, *A&A*, **554**, A103
- Pineda J. E., et al., 2022, *arXiv e-prints*, p. arXiv:2205.03935
- Pon A., Johnstone D., Heitsch F., 2011, *ApJ*, **740**, 88
- Ragan S. E., Henning T., Tackenberg J., Beuther H., Johnston K. G., Kainulainen J., Linz H., 2014, *A&A*, **568**, A73
- Rawat V., et al., 2023, *MNRAS*, **521**, 2786
- Rodríguez-Franco A., Martín-Pintado J., Gómez-González J., Planesas P., 1992, *A&A*, **264**, 592
- Roman-Duval J., Jackson J. M., Heyer M., Rathborne J., Simon R., 2010, *ApJ*, **723**, 492
- Romero G. A., Cappa C. E., 2009, *MNRAS*, **395**, 2095
- Rosolowsky E. W., Pineda J. E., Kauffmann J., Goodman A. A., 2008, *ApJ*, **679**, 1338
- Saha A., et al., 2022, *MNRAS*, **516**, 1983
- Sanhueza P., et al., 2019, *ApJ*, **886**, 102
- Savage C., Apponi A. J., Ziurys L. M., Wyckoff S., 2002, *ApJ*, **578**, 211
- Schisano E., et al., 2014, *ApJ*, **791**, 27
- Schneider N., Csengeri T., Bontemps S., Motte F., Simon R., Hennebelle P., Federrath C., Klessen R., 2010, *A&A*, **520**, A49
- Schuller F., et al., 2021, *MNRAS*, **500**, 3064
- Shan W., et al., 2012, *IEEE Transactions on Terahertz Science and Technology*, **2**, 593
- Shimajiri Y., et al., 2015, *ApJS*, **217**, 7
- Shimajiri Y., André P., Palmeirim P., Arzoumanian D., Bracco A., Könyves V., Ntormousi E., Ladjelate B., 2019, *A&A*, **623**, A16
- Smith R. J., Glover S. C. O., Klessen R. S., 2014, *MNRAS*, **445**, 2900
- Su Y., et al., 2019, *ApJS*, **240**, 9
- Suri S., et al., 2019, *A&A*, **623**, A142
- Tigé J., et al., 2017, *A&A*, **602**, A77
- Treviño-Morales S. P., et al., 2019, *A&A*, **629**, A81
- Urquhart J. S., et al., 2008, *A&A*, **487**, 253
- Vázquez-Semadeni E., Gómez G. C., Jappsen A. K., Ballesteros-Paredes J., Klessen R. S., 2009, *ApJ*, **707**, 1023
- Vázquez-Semadeni E., Palau A., Ballesteros-Paredes J., Gómez G. C., Zamora-Avilés M., 2019, *MNRAS*, **490**, 3061
- Walker D. L., Longmore S. N., Bastian N., Kruijssen J. M. D., Rathborne J. M., Galván-Madrid R., Liu H. B., 2016, *MNRAS*, **457**, 4536
- Wang K., Testi L., Ginsburg A., Walmsley C. M., Molinari S., Schisano E., 2015, *MNRAS*, **450**, 4043
- Wang K., Testi L., Burkert A., Walmsley C. M., Beuther H., Henning T., 2016, *ApJS*, **226**, 9
- Wilson T. L., Rood R., 1994, *ARA&A*, **32**, 191
- Wouterloot J. G. A., Brand J., 1989, *A&AS*, **80**, 149
- Xu J.-L., Xu Y., Zhang C.-P., Liu X.-L., Yu N., Ning C.-C., Ju B.-G., 2018, *A&A*, **609**, A43
- Yang D., et al., 2023, *ApJ*, **953**, 40
- Yuan J., et al., 2018, *ApJ*, **852**, 12
- Zavagno A., et al., 2023, *A&A*, **669**, A120
- Zernicke A., 2015, PhD thesis, University of Cologne, Institute for Physics
- Zhang M., Kainulainen J., Mattern M., Fang M., Henning T., 2019, *A&A*, **622**, A52
- Zhang S., et al., 2023, *MNRAS*, **520**, 322
- Zhou J.-W., et al., 2022, *MNRAS*, **514**, 6038
- Zhou J. W., et al., 2023, *arXiv e-prints*, p. arXiv:2305.12573

APPENDIX A: FILFINDER ALGORITHM AND LARGE-SCALE FILAMENTS

The *FilFinder* package picks out the structures within a given mask by comparing each pixel to those in the surrounding neighbourhood using adapting thresholding. The algorithm then reduces the filament mask to skeletons using the Medial Axis Transform (MAT) method. Finally, it prunes down the skeleton structure to a filamentary network. *Filfinder* not only extracts bright filaments but also reliably extracts fainter structures such as striations. We set the following optimum values in *Filfinder* for creating mask and applying adapting thresholding, whose output matches better with the elongated structures visually seen in the column density map: i) global threshold, the intensities below this value are cut off from being included in the mask, as two times the background column density value, ii) adaptive threshold, the expected full width of filaments for adaptive thresholding, as 10 pixels (i.e. ~ 5 times beam-width), iii) smooth size, used to smoothen the image to minimize the extraneous branches on the skeletons as 2 pixels (i.e. ~ 1.0 times beam-width), iv) size threshold, the minimum dimensions expected for a filament as 100 pixels² (i.e. ~ 20 times beam area). The emission structures were first flattened to 95 percentiles before applying the adapting thresholding to suppress the significantly brighter objects than filamentary structures such as dense cores.

APPENDIX B: RADFIL AND FILAMENT PROFILES

We employed *RadFil* to find the filament radial profile, width, and other properties. *RadFil* first smooths the filament spine and then makes perpendicular cuts to the tangent lines sampled evenly across the smoothed filament (see Fig. 12a and A1). Each cut is shifted to the peak intensity along the cut, which is marked by the blue dots in Fig. 12a and A1. Then, it computes the radial distances from the peak intensity point and the corresponding pixel intensities for each intersecting pixel along a given cut (see Zucker & Chen 2018). In this way, *RadFil* generates the intensity profile of each cut. Following the procedure, we made equidistant cuts perpendicular to the spine using a sampling frequency of 1 beam size. The radial profile at each cut was extracted, which gives an average profile or master profile of the filament and is shown in Fig. 12b and B1.

We identified the filament width (FWHM) by fitting a Gaussian function on the entire ensemble of the cuts. Before fitting the profile, a background was subtracted using the background subtraction estimator of *RadFil* (Zucker & Chen 2018). The background was estimated using the first-order polynomial for all the profiles at a given radial distance from the centre pixel (highest intensity pixel). The radial distance for background estimation is taken in the range where the observed intensity of the radial profile seems to be at a constant level for the filaments. The best-fit parameters are given in Table 2.

This paper has been typeset from a \LaTeX file prepared by the author.

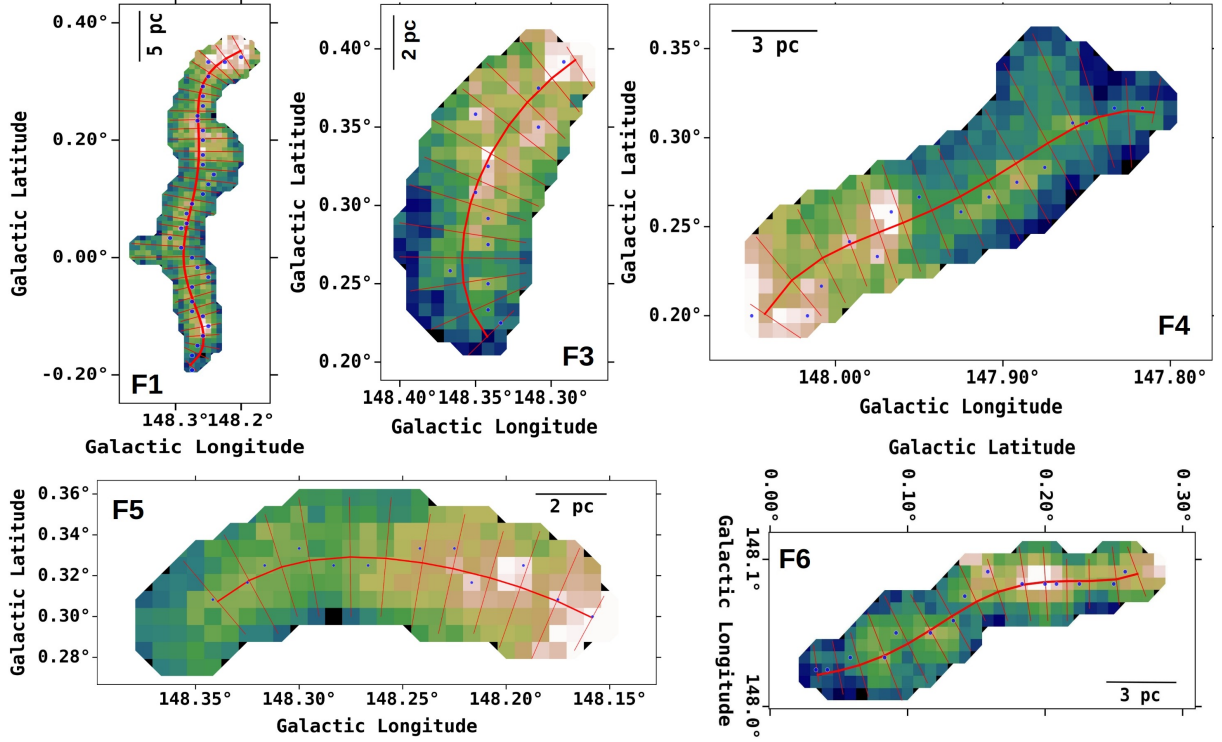


Figure A1. The filaments spines (red curve) of F1, F3, F4, F5, and F6 shown over there ^{13}CO integrated intensity emission. The blue dots are the same as in Fig. 12a.

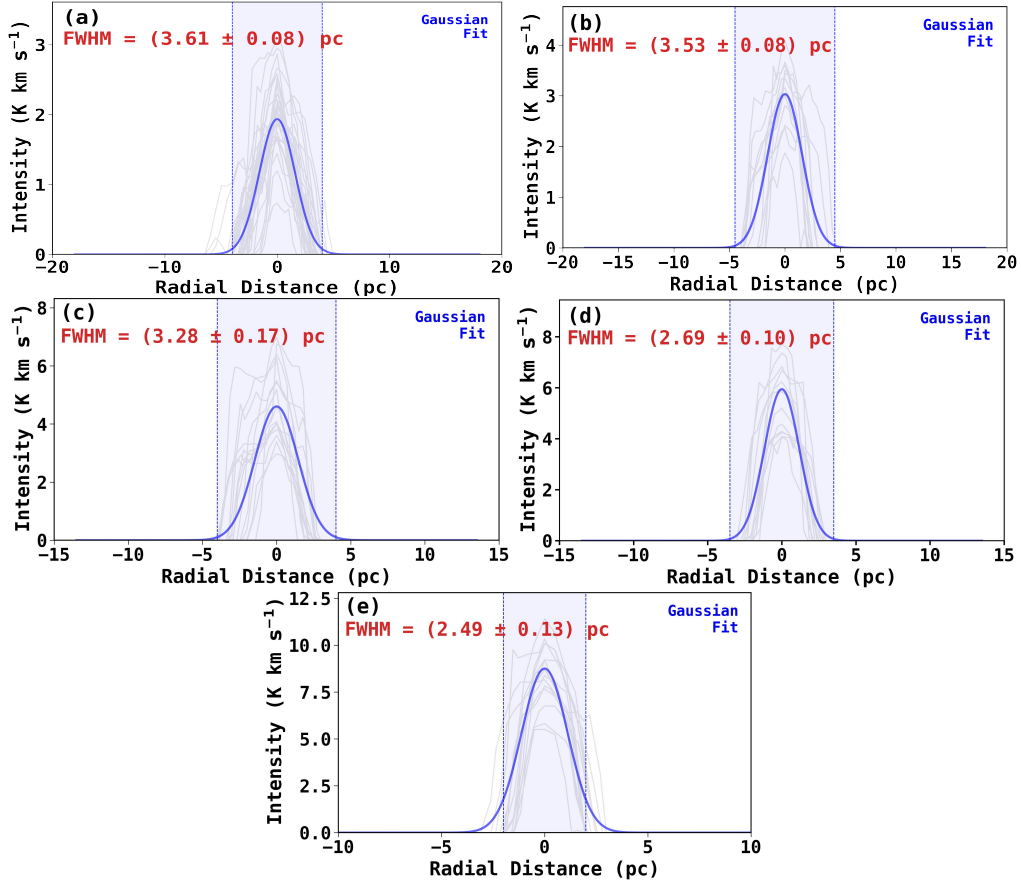


Figure B1. The radial profiles of perpendicular cuts along the filament spines of (a) F1, (b) F3, (c) F4, (d) F5, and (e) F6, with details same as in Fig. 12b.